



## Dynamics of a Taylor bubble in steady and pulsatile co-current flow of Newtonian and shear-thinning liquids in a vertical tube



S. Abishek <sup>a,\*</sup>, A.J.C. King <sup>b,1</sup>, R. Narayanaswamy <sup>b,2</sup>

<sup>a</sup> Sustainable Engineering Group, Curtin University, Perth, Australia

<sup>b</sup> Department of Mechanical Engineering, Curtin University, Perth, Australia

### ARTICLE INFO

#### Article history:

Received 23 September 2014

Received in revised form 16 March 2015

Accepted 27 April 2015

Available online 8 May 2015

**Keywords:**  
Taylor bubble  
Shear-thinning  
Pulsatile  
Co-current  
Non-Newtonian  
Multiphase

### ABSTRACT

A computational analysis is carried out to ascertain the effects of steady and pulsatile co-current flow on the dynamics of an air bubble rising in a vertical tube containing water or a solution of Carboxymethylcellulose (CMC) in water. The mass fraction ( $m_f$ ) of CMC in the solution is varied in the range  $0.1\% \leq m_f \leq 1\%$  to accommodate zero-shear dynamic viscosities in the range  $0.009\text{--}2.99 \text{ Pa}\cdot\text{s}$ . It was found that the transient and time-averaged velocities of Taylor bubbles are independent of the bubble size under both steady as well as pulsatile co-current flows. The lengths of the Taylor bubbles under the Newtonian conditions are found to be consistently greater than the corresponding shear-thinning non-Newtonian conditions for any given zero-shear dynamic viscosity of the liquid. In contrast to observations in stagnant liquid columns, an increase in the dynamic viscosity of the liquid (under Newtonian conditions) results in a concomitant increase in the bubble velocity, for any given co-current liquid velocity. In shear-thinning liquids, the change in the bubble velocity with an increase in  $m_f$  is found to be relatively greater at higher co-current liquid velocities. During pulsatile shear-thinning flows, distinct ripples are observed to occur on the bubble surface at higher values of  $m_f$ , the locations of which remain stationary with reference to the tube for any given pulsatile flow frequency, while the bubble propagated upwards. In such a pulsatile shear-thinning flow, a localised increase in dynamic viscosity is accompanied near each ripple, which results in a localised re-circulation region inside the bubble, unlike a single re-circulation region that occurs in Newtonian liquids, or shear-thinning liquids with low values of  $m_f$ . It is also seen that as compared to frequency, the amplitude of pulsatile flow has a greater influence on the oscillating characteristics of the rising Taylor bubble. The amplitude of oscillation in the bubble velocity increases with an increase in the CMC mass fraction, for any given value of pulsatile flow amplitude.

© 2015 Elsevier Ltd. All rights reserved.

### Introduction

Many industrial, natural and biological systems are observed to have flows where large contiguous bubbles (Taylor bubbles) travel in comparably narrow passages filled with liquid – a flow regime typically identified as slug flow. Examples include phase-change

\* Corresponding author at: Building 603, Sustainable Engineering Group, Curtin University, No. 6, Sarich Way, Bentley, Western Australia 6102, Australia. Tel.: +61 8 9266 9974; fax: +61 8 9266 2681.

E-mail addresses: abishek1986@gmail.com (S. Abishek), Andrew.King@curtin.edu.au (A.J.C. King), R.Narayanaswamy@curtin.edu.au (R. Narayanaswamy).

<sup>1</sup> Address: Building 204, Department of Mechanical Engineering, Curtin University, Kent Street, Bentley, Western Australia 6102, Australia. Tel.: +61 8 9266 7661; fax: +61 8 9266 2681.

<sup>2</sup> Address: Building 204, Department of Mechanical Engineering, Curtin University, Kent Street, Bentley, Western Australia 6102, Australia. Tel.: +61 8 9266 4483; fax: +61 8 9266 2681.

cooling systems, oil and gas transport systems, mud-volcanoes, food processing equipment, reverse osmosis systems and emboli in blood streams. In columns or tubes with stationary liquids, the rise velocity of an entrapped bubble is governed by the buoyancy, volume of the bubble, size of the tube and the fluid (viscosity and surface tension), while the mean velocity of the liquid becomes an additional controlling parameter for bubbles rising in flowing liquids.

The dynamics of Taylor bubbles in stationary and flowing liquids have been studied in considerable detail since the 1940s (Dumitrescu, 1943). Davies and Taylor (1950) carried out one of the earliest analytical and experimental studies on elongated Taylor bubbles rising in stagnant liquids and showed that the rise velocity of Taylor bubble in a liquid-filled tube is proportional to  $\sqrt{gd}$  where  $d$  is the diameter of the tube. Uno and Kintner (1956) carried out experimental studies to determine the rise

velocity of air bubbles in quiescent liquids (for a wide range of liquid viscosities and surface tensions) in a vertical tube ( $2.09 < d < 15.25$  cm). They correlated the rise velocity of the bubble in terms of the velocity of an equivalent sphere moving in the liquid, corrected by a factor that depended on the diameter of the tube and interfacial surface tension, and independent of liquid viscosity. Maeda (1975) carried out experiments on the rise velocity of spherical and Taylor bubbles in stationary and flowing liquids (air–water systems) inside vertical cylindrical tubes. They showed that in quiescent liquids, there is a critical diameter (depending on the bubble size) of the tube below which the bubble may not rise freely. In flowing liquids, they showed that the bubble rise velocity is a linear function of the liquid velocity and the velocity of rise of bubble in a stationary liquid (given by Davies and Taylor, 1950). They suggested that the balance of buoyancy and drag is the primary mechanism determining the kinetics of smaller spherical and ellipsoidal bubbles, while Taylor instability on the bubble surface controlled the dynamics of Taylor bubbles.

Quan (2011) carried out computational analysis on the effects of co-current (both upward and downward flows) liquid velocities on the dynamics of a rising Taylor bubble for a range of Archimedes numbers ( $Ar = \rho_l [\rho_l - \rho_b] g d^3 / \mu_l^2$ ). It was shown that during upward liquid flows, the tail of the bubble elongates and may even oscillate with an increase in Ar, while the downward liquid flow tends to shorten the bubble, and even lead to a rounded shape at the rear of the bubble under sufficiently high liquid velocities. They confirmed that during both upward as well as downward directions of the liquid flow, the terminal velocity of the bubble could be related in terms of the mean liquid velocity and the bubble rise velocity in quiescent liquid as given by Maeda (1975). Kang et al. (2010) carried out similar computational simulations using a front-tracking Volume-Of-Fluid (VOF) technique and concluded that the Eotvos number ( $Eo$ ) and Archimedes number ( $Ar$ ) significantly influenced the shape of the bubble; greater  $Eo$  and  $Ar$  resulted in longer bubble tail and a larger wake behind the bubble. In a recent experimental study on slug flows, Kajero et al. (2012) characterised the effects of viscosity over the range 5–5000 m Pa·s on the length of Taylor bubbles, liquid film thickness, pressure gradients, and slug intermittencies, for superficial gas velocities in the range 0.02–0.361 m/s. They pointed out that the length of Taylor bubbles, the liquid film thickness adjacent to the bubble, and the pressure gradient in the slug, increase whereas the slug frequency and length of liquid slug decrease with an increase in liquid viscosity. Nogueira et al. (2005) employed particle image velocimetry (PIV) and pulsed shadowgraphy to study the effects of liquid viscosity on the flow-field and dynamics of a Taylor bubble rising in stagnant and co-current flows in a vertical tube. Different aqueous solutions of glycerol were used to obtain liquid viscosities in the range of  $10^{-3}$ –1.5 Pa·s. It was reported that the inverse viscosity number ( $Ar^{0.5}$ ), and the Reynolds number based on the liquid velocity relative to the bubble, dictate the wake flow patterns behind the bubble under stagnant and co-current liquid conditions, respectively. It was also found that the length of the wake behind the Taylor bubble was solely depended on  $Ar^{0.5}$  and increased with an increase in  $Ar^{0.5}$  for stagnant liquid conditions, while the dependency was with the relative Reynolds number for co-current flow conditions. They also identified that the laminar-turbulent transition in the wake occurs for the relative Reynolds number in the range 175–575.

Some of the aforementioned studies highlighted the effects of viscosity on the dynamics of Taylor bubbles, typically from studies using different liquids. However, the understanding of bubble dynamics in non-Newtonian liquids (generally shear thinning or viscoelastic rheology) is important in several industrial applications including food processing (aeration of molten chocolate), de-aeration of paints, oil exploration and drilling applications,

and biological systems such as blood embolism (Johnson and White, 1993). Despite the relevance to industrial, natural and biological processes, the literature on the dynamics of Taylor bubbles in non-Newtonian liquids is very limited, and much of the literature on the bubble dynamics that is available deals with nearly-spherical bubbles (Herrera-Velarde et al., 2003; Hassager, 1979; Margaritis et al., 1999; Li et al., 2012; Amirnia et al., 2013; Funfschilling and Li, 2001).

Sousa et al. (2005) carried out experiments using PIV and shadowgraphy to determine the flow field and velocity of Taylor bubbles rising in stagnant non-Newtonian solutions of Carboxymethylcellulose (CMC) in water, which predominantly had a shear-thinning rheology for the concentrations they considered. It was reported that the shape of bubble nose remained almost identical for the range of CMC mass fractions studied (0.1–1%), while the shape of the bubble tail varied significantly. They pointed out that with an increase in the solution viscosity, the wake flow pattern varied from turbulent to laminar, and a negative wake was observed for the higher CMC mass fractions. An increase in  $m_f$  was found to decrease the rise velocity of Taylor bubbles in stagnant liquids. In a subsequent study, Sousa et al. (2007) reported that for relatively lower mass fractions of CMC or polyacrylamide, the interaction between Taylor bubbles was similar to that found in Newtonian fluids, while for  $m_f = 1\%$  (CMC solution), a negative wake formed behind the Taylor bubbles, inhibiting coalescence in the bubbles. Carew et al. (1995) carried out experimental studies on rising Taylor bubbles in Newtonian and shear-thinning liquids in inclined tubes. They showed that an increase in the liquid viscosity or increase in surface tension caused the nose region of the bubbles to become blunt and resulted in a reduction in the bubble rise velocities.

Pulsatile non-Newtonian flows with entrapped bubbles occur when gas emboli get into the blood stream in circumstances such as accidental introduction during cardio-vascular surgeries or during decompression sickness. Bubbles are also introduced into the blood stream deliberately to block the blood supply to tumours in blood vessels. In an ongoing experimental research by the authors, it was found that introduction of pulsations in the fluid velocity can result in the breakup of entrapped bubbles in closed loop fluid systems which require gas evacuation. Pulsatile slug flows with elongated Taylor bubbles are also found in advanced high performance heat sinks such as pulsating heat pipes (Tong et al., 2001).

A survey of the literature reveals that there are significant reports on the dynamics of Taylor bubbles rising in stationary and co-currently flowing Newtonian liquids, and there have been some recent studies involving non-Newtonian liquids. It is well known that the introduction of flow pulsations result in complex fluid dynamic behaviour in both Newtonian as well as non-Newtonian liquids, however, the influence on entrapped Taylor bubbles is largely unexplored. Separate to pulsatile flows with entrapped bubbles, there has been some recent interest in the study of Taylor bubbles in oscillating tubes, undergoing vibration (transporting two-phase mixtures). Brannock and Kubie (1996) carried out one of the earliest studies on the effect of wall oscillations on the rise velocity of Taylor bubbles. They found that bubble rise velocity decreased with an increase in vibration–acceleration, and identified a critical acceleration for complete bubble breakup. In a subsequent study, Kubie (2000) reported that horizontal vibrations applied to the tube resulted in an increase in the bubble velocity for an increase in vibration–acceleration. From a similar study, Madani et al. (2009) observed that, for weak wall accelerations, the mean bubble rise velocity decreases with the vibration–acceleration, and there existed a critical acceleration beyond which the average bubble velocity increased while the fluctuating bubble velocity decreased. They also noticed that

capillary waves that originated at the nose of the Taylor bubble and propagated downwards along the bubble when wall oscillations were present. Such capillary waves have also been observed in conditions without wall oscillations, primarily due the unsteady oscillations in the tail of the bubble that propagate upwards along the direction of bubble rise (Liberzon et al., 2006).

Pulsatile liquid flows with entrapped bubbles in tubes, can potentially result in bubble shape oscillations, and even bubble disintegration depending on the characteristics of the pulsatile liquid velocity. Considering that the characteristics of pulsatile flows of shear-thinning liquids are significantly different from that of Newtonian liquids in tubes (El-Sayed, 1984), the dynamics of Taylor bubbles in pulsatile non-Newtonian liquid systems can be vastly different to that in Newtonian liquids, due to the local viscosity variations. It is reasonable to say that there has been no detailed analysis of the effects co-current flow pulsations on the dynamics of Taylor bubbles in pulsatile Newtonian or non-Newtonian flows. With this motivation, the present research deals with a fundamental study that aims to understand the dynamics of Taylor bubbles in co-current steady and pulsatile flow of Newtonian and shear-thinning liquids in a vertical tube. Two different types of two-phase fluid systems are considered for the study: (i) air bubbles in water; and (ii) air bubbles in CMC-water solution.

### Problem description, geometry and computational domain

A schematic of the tube geometry considered for the present study is shown in Fig. 1(a) and the corresponding computational mesh for a representative section of the tube is shown in Fig. 1(b). As shown in the figure, the physical domain consists of a tube of length,  $l$  and diameter,  $d$ , that includes an inlet and an outlet through which water or CMC solution flows, with an entrapped bubble of known volume (or equivalent diameter  $d_e$ ). A fully developed velocity profile determined from a separate simulation is imposed at the inlet of the tube for steady flows, while a sinusoidal oscillation (dimensionless amplitude  $A$ , and frequency,  $f$ ) about the fully developed mean velocity profile is imposed for pulsating flow conditions to represent a sinusoidal variation in mass flow rate with time. The dimensionless pulsatile flow amplitude is defined as the ratio of the pulsatile velocity amplitude to the mean velocity of the liquid. It is realised that the fully developed pulsating flow velocity profile does not resemble a proportional variation in the local velocity with the imposed mass-flow pulsation (El-Sayed, 1984; Haddad et al., 2010), and may even result in local flow reversals for certain ranges of frequencies and amplitudes of pulsation. Hence, a series of simulations were performed to determine the entrance length

(distance from the inlet before the flow becomes hydrodynamically fully developed) during pulsating flow. For the range of pulsation frequencies, amplitudes, flow rates and fluids considered for the present study, the entrance length is determined to be less than  $20 \times d$  from the inlet, when the oscillating velocity profile is imposed at the tube-inlet. It is ensured that the total length of the tube ( $l = 1.2$  m) considered for the simulations is long enough to accommodate this entrance length and also for the bubble to reach terminal velocity during steady flow or oscillating terminal velocity during pulsating flow. A representative typical pulsating velocity imposed at the inlet of the tube, and the fully developed spatial velocity distribution obtained at a certain distance downstream, during different phases of a pulsation cycle is shown in Fig. 2(a). The corresponding entrance length can be identified from the velocity gradient (given by  $\partial u_z / \partial z|_{x=0}$ ) along the direction of the tube axis from Fig. 2(b).

While the schematic shown in Fig. 1(a) represents an axisymmetric cylindrical tube, an equivalent full 3D tube geometry is also employed for the simulation of some cases considered for the present study that involve bubble diameters smaller than the diameter of the tube, to ensure accurate prediction of the three-dimensional flow physics. It is seen that, for larger bubble diameters (Taylor bubbles), the computational predictions including the bubble shape and bubble rise velocities from the 2D axisymmetric simulations were in excellent agreement with those obtained using full scale 3D simulations. A quantitative comparison is provided later in section ‘Validation’ of this paper. As shown in Fig. 1(b), a fully structured spatially varying non-uniform mesh is used for the simulations, where the mesh is finer near the wall, and uniform along the axis of the tube. For the 3D simulations, a hexahedral mesh is used with runtime mesh refinement about the liquid–bubble interface. The mesh used for the simulation of the results reported in the present study was determined from a detailed grid sensitivity analysis.

### Methodology

The governing equations for the conservation of mass and momentum are solved using the finite-volume based *interFoam*/*interDyMFoam* solver in OpenFOAM-2.1. The *interDyMFoam* solver uses the same formulation as the *interFoam* solver, but facilitates adaptive mesh refinement. The solvers use an algebraic volume-of-fluid (VOF) approach which is well-established for simulation of flows where two immiscible fluids are present and a distinct surface interface can be defined. In VOF approaches, the different phases (liquid and air in the present work) are represented in the domain in terms of their volume fraction as:

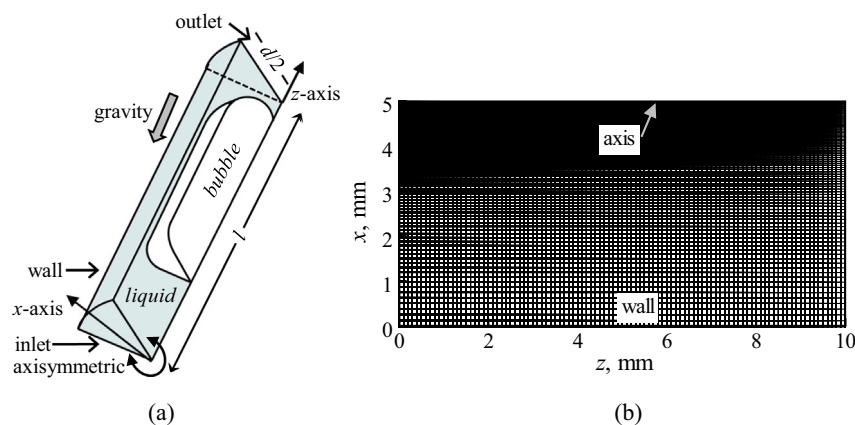


**Fig. 1.** Schematic of the axisymmetric (a) geometry of the tube, and coordinate system used for the present study and (b) typical mesh for a section of the tube.

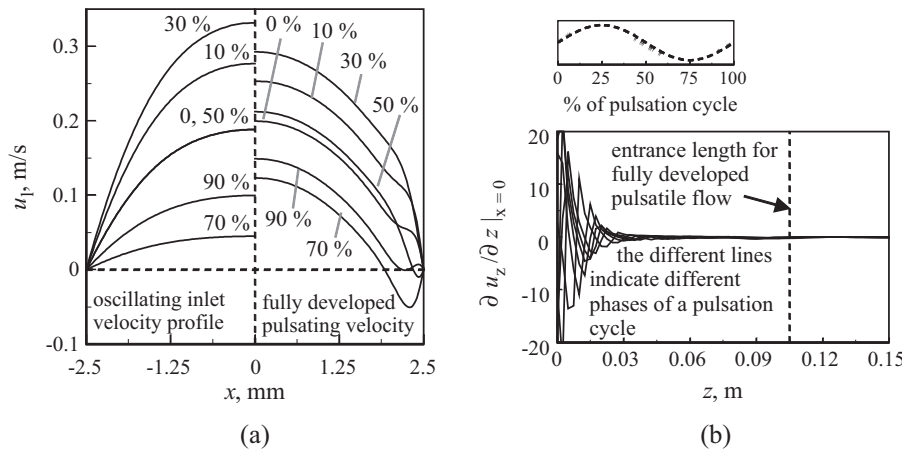


**Fig. 2.** Typical fully developed velocity distribution during pulsatile flow of water in a pipe;  $d_e = 5$  mm,  $Re = 600$ ,  $A = 0.8$ , and  $f = 10$  Hz.

$$\alpha_b = 1 - \alpha_l \quad (1)$$

The subscripts l and b correspond to the liquid and bubble, respectively. A single equation for each, mass (continuity) and momentum conservation, is used to describe the system, using the properties (density and viscosity) determined locally in the domain based on the properties of each phase, and the local volume fraction as follows:

$$\text{Continuity: } \nabla \cdot \vec{u} = 0 \quad (2)$$

$$\begin{aligned} \text{Momentum: } & \partial(\rho \vec{u}) / \partial t + \nabla \cdot (\rho \vec{u} \vec{u}) \\ & = -\nabla p + \nabla \cdot (\mu \nabla \vec{u}) + \rho \vec{g} + f_\sigma \end{aligned} \quad (3)$$

A separate transport equation is solved for the volume fraction as,

$$\partial \alpha_l / \partial t + \nabla \cdot (\alpha_l \vec{u}) + \nabla \cdot [\vec{u}_c \alpha_l (1 - \alpha_l)] = 0 \quad (4)$$

where  $\vec{u}_c$  is designated as the compression velocity. This is an additional term included in the conservation equations to ensure a sharply defined interface between the liquid and gas phases. The VOF implementation in *interFoam*/ *interDyMFoam* is an algebraic VOF method, and geometric reconstruction of the interface is not performed. In the preceding Eqs. (1)–(4), the equivalent fluid density and viscosity are given in terms of the local volume fraction as:

$$\rho = \alpha_l \rho_l + \alpha_b \rho_b \text{ and } \mu = \alpha_l \mu_l + \alpha_b \mu_b \quad (5)$$

The source term  $f_\sigma$  in Eq. (3) represents the interfacial surface tension force density that exists at the interface ( $0 < \alpha_l < 1$ ) and  $f_\sigma = 0$  everywhere else in the domain. This source term is included in the momentum equation to alleviate the computational issues associated with a sharp pressure jump that exists across the liquid–gas interface. In the present VOF methodology,  $f_\sigma$  is based on the continuum-surface-force model introduced by Brackbill et al. (1992), as follows:

$$f_\sigma = -\sigma [\nabla \cdot (\nabla \alpha_l / |\nabla \alpha_l|)] (\nabla \alpha_l) \quad (6)$$

Deshpande et al. (2012) provide a thorough description and VOF implementation in *interFoam*, along with extensive validation of the solver. The multiphase continuity and momentum equations are solved using a merged PISO-SIMPLE algorithm, while the Multidimensional Universal Limiter with Explicit Solution (MULES) algorithm is employed for the volume-fraction transport equation. This algorithm is an iterative flux-corrected transport scheme (extended from Zalesak, 1979; Ubbink, 1997; Ubbink and Issa, 1999). No special treatment of the wall was required as the bubble did not wet the wall, for the operating conditions and range of parameters considered.

The instantaneous bubble velocity ( $u_b$ ) in the direction along the axis of the tube ( $z$ -axis, direction of bubble rise) is obtained by numerically differentiating the position vector of the centre-of-mass of the bubble ( $z_b$ ), with time; where  $z_b$  is obtained by a volume fraction-weighted average of the cell centres over the domain, containing the bubble. The position of the centre of mass of the bubble along the  $z$ -axis, and the instantaneous velocity for a representative case is shown in Fig. 3.

To isolate the effects of shear thinning rheology of the liquid alone, on the bubble dynamics, viscoelasticity of the CMC solution is not considered in the present study. In support of this assumption – Benchabane and Bekkour (2008) conducted extensive experiments to characterise the rheology of CMC solutions for CMC mass fractions in the range 0.2–6%, and noted that the viscoelastic effects only become significant only beyond a CMC mass fraction of about 2.5%. Several other studies including Acharya and Ulbrecht (1978) and Sousa et al. (2007) also pointed out that the viscoelastic properties of CMC solutions are unimportant for low mass fractions, of the order considered in the present study (0–1%). Hence, all further mention of “non-Newtonian” behaviour of the fluid considered in the present research refer to the “shear-thinning non-Newtonian” behaviour of the CMC solution.

The properties used in the present study for water, CMC solutions and air (bubble phase) are shown in Table 1. The dynamic viscosities of the shear-thinning CMC solutions used in Eqs. (3) and (5) are determined from the Carreau–Yasuda viscosity model, following Sousa et al. (2005) as:

$$\mu_l = \mu_{l,0} + (\mu_{l,0} - \mu_\infty) [1 + (\lambda \cdot \dot{\gamma})^{C_1}]^{(C_2-1)/C_1} \quad (7)$$

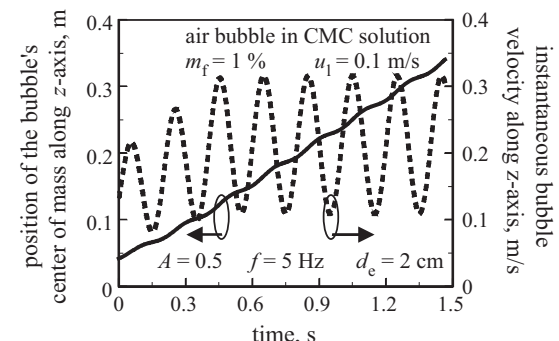


**Fig. 3.** Instantaneous position and velocity of the bubble's centre of mass for a representative case of an air bubble rising in a CMC solution in pulsatile flow.

**Table 1**

Material properties used for the present study.

Fluid	$\rho$ , kg/m <sup>3</sup>	$\sigma$ , N/m	$\mu_{l,0}$ , Pa-s	$\mu_{l,\infty}$ , Pa-s	$\lambda$ , s	$C_1$ , –	$C_2$ , –	$\dot{\gamma}$ , 1/s	Reference
Water	996.58	0.072	$8.684 \times 10^{-4}$	–	–	–	–	–	R1
0.1% by mass of CMC in water	996.283	0.0725	0.009	0.001	0.021	0.850	0.871	1–4000	R2, R3
0.4% by mass of CMC in water	995.394	0.0722	0.110	0.001	0.110	0.809	0.675	0.125–4000	R2, R3
1% by mass of CMC in water	993.614	0.0715	2.990	0.001	0.365	0.668	0.400	0.04–4000	R2, R3
Air (bubble)	1.1845	–	$1.557 \times 10^{-5}$	–	–	–	–	–	–

Note:  $\sigma$  represents the surface tension of the liquid-air interface.

R1 – NIST Standard Reference Database.

R2 – Sousa et al. (2005).

R3 – Lee et al. (2012).

where  $\dot{\gamma}$  is the local strain rate ( $s^{-1}$ ),  $\mu_{l,0}$  and  $\mu_{l,\infty}$  are the dynamic viscosity at zero and infinite shear, respectively, and  $\lambda$ ,  $C_1$  and  $C_2$  are constants. The values for surface tension ( $\sigma$ ) of CMC solutions (with air), at different mass fractions, shown in Table 1 is obtained from Lee et al. (2012). The density of the CMC solution is determined as:

$$\rho_l = m_f \cdot \rho_{CMC} + (1 - m_f) \cdot \rho_w \quad (8)$$

where  $m_f$  is the mass fraction of CMC in water, and  $\rho_{CMC}$  and  $\rho_w$  are the densities of CMC and water respectively.

All computational simulations were carried out using 320–480 cores on the supercomputing facility Magnus with a Cray XC30 system, at iVEC Pawsey Supercomputer Centre, Perth, Australia.

## Results and discussion

The results from computational analysis on the dynamics of a Taylor bubble rising through a vertical cylindrical tube, during assisted (against the direction of gravity) steady or pulsatile flow of water (Newtonian) or CMC solution (shear-thinning) is presented. The range of operating conditions considered for the present study is given in Table 2. The range of velocities, bubble and tube diameters, and fluids are chosen based on the operating ranges for which the computational methodology is validated (delineated in section ‘Validation’).

### Validation

The present computational methodology is extensively validated for both Newtonian as well as shear-thinning (power law) fluids, by comparison of the predicted bubble shape, bubble velocity, liquid film thickness, and liquid and gas velocities, against analytical, experimental and computational results in the literature (Maeda, 1975; Marschall et al., 2014; Chhabra and Richardson, 1999; Hewson et al., 2009; Kamisli and Ryan, 1999).

The first set of experimental data pertains to a freely rising air bubble (of different sizes) in a vertical cylindrical tube filled with water (Maeda, 1975). The comparison of the variation in the predicted bubble rise velocity for different equivalent bubble diameters against the experimental data is shown in Fig. 4(a). It is seen

from the figure that there is excellent agreement between the present simulations and experiment with a maximum error of 4%.

The second experimental data set pertains to an elongated Taylor bubble rising in a vertical square (cross-section) capillary tube with co-current flow of water (Marschall et al., 2014). Fig. 4(b) shows the comparison between the present results and the experimental bubble shapes obtained in the plane along the diagonal to the square cross-section of the channel. As can be seen in the figure, the maximum deviation between the predicted and experimental bubble shapes is less than 1%. This simulation was carried out on a three dimensional mesh, though the comparisons of the bubble shapes on other cross-sectional planes are omitted here for brevity; over all cross-sections, the maximum error in the predicted bubble length was under 1% compared with the experimental results from Marschall et al. (2014).

As mentioned in the preceding section, the computational methodology employed in the present research uses an algebraic VOF formulation, and additional validation is undertaken to ascertain its accuracy for multiphase flows involving shear thinning fluid rheologies. The first of these validations consider a pressure driven flow of a Newtonian and shear-thinning (power-law) fluid between two fixed walls. The simulation results are compared against the analytical solution (Chhabra and Richardson, 1999) for the velocity profiles in each fluid. The fluid properties considered are: density (for both fluids) = 1 kg/m<sup>3</sup>, the dynamic viscosity of the Newtonian fluid is  $10^{-3}$  Pa-s, and the effective apparent local dynamic viscosity of the power-law fluid is defined using:

$$\mu_{app, l} = K \dot{\gamma}^{n-1} \text{ and } \tau = K \dot{\gamma}^n \quad (9)$$

where  $\tau$  is the shear stress,  $\dot{\gamma}$  is the strain rate in the fluid,  $K$  is the flow-consistency-index ( $=0.05$  Pa-s<sup>n</sup>), and  $n$  is the power-law index ( $=0.5$ ). Further assumptions and details of the analytical solution for the velocity profiles can also be found in Focke and Bothe (2011). For the purpose of comparison, the predictions from a coarse and fine mesh are shown in Fig. 4(c). It is seen from figure that the magnitude of velocity predicted from the present simulations and the analytical results are in excellent agreement, with a maximum deviance of less than 1%.

The final validation case identified from the literature considers the liquid film thickness obtained during the motion of a bubble in

**Table 2**

Range of parameters considered for the present study.

Bubble–liquid combination	$d$ , mm	$m_f$ , %	$u_l$ , m/s	$A$ , –	$f$ , Hz	$d_e$ , mm
Air bubble in water	5	–	0.1046 (Re = 600)	Steady, 0.25, 0.5, 1,	Steady, 1, 5, 10, 30, 40	2, 6, 10
Air bubble in CMC solution (Newtonian-treatment)	10	0.1, 0.4, 1	0.1, 0.4	Steady	Steady	10, 20
Air bubble in CMC solution	10	0.1, 1	0.1, 0.4	Steady, 0.5, 1	Steady, 5, 10	20

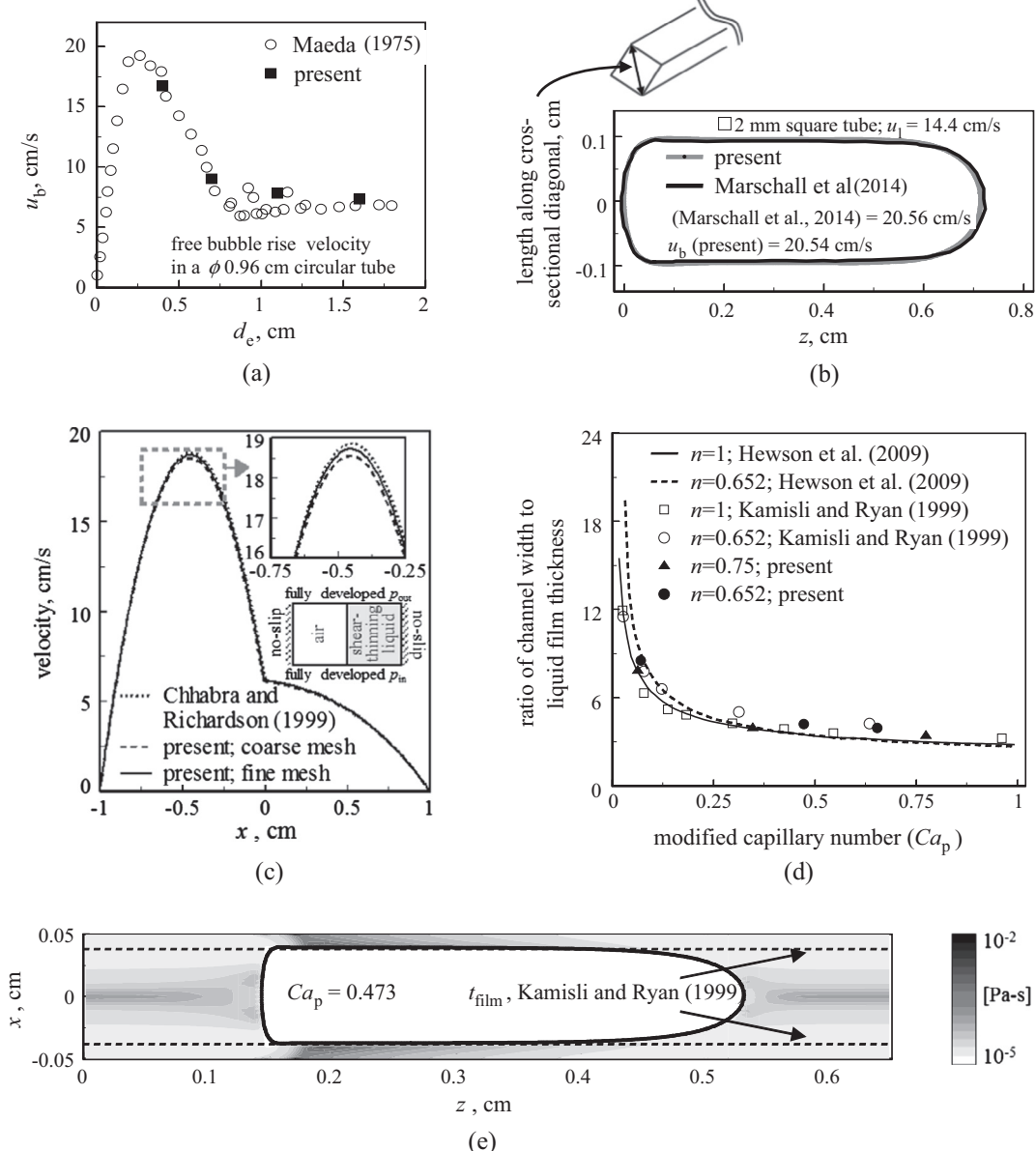


**Fig. 4.** Comparison of (a) predicted terminal velocity of bubble against experimental data (Maeda, 1975); (b) predicted bubble shape against experimental data (Marschall et al., 2014); (c) predicted liquid and gas velocity against analytical result (Chhabra and Richardson, 1999); (d) predicted dimensionless liquid film thickness against Hewson et al. (2009) and Kamisli and Ryan (1999), and (e) predicted counters of dynamic viscosity and bubble shape superimposed on the asymptotic liquid film thickness from Kamisli and Ryan (1999).

a shear thinning (power-law) fluid and is analogous to a shear-thinning liquid drawn out by a moving plate (Hewson et al., 2009; Kamisli and Ryan, 1999). For this validation, two dimensional simulations are carried out for the pressure driven motion of a neutrally-buoyant elongated bubble, in a shear-thinning power-law liquid. The width of the channel considered 1 mm, \$\rho\_1 = \rho\_0 = 1000 \text{ kg/m}^3\$, and \$\mu\_b = 10^{-5} \text{ Pa}\cdot\text{s}\$. The shear-thinning behaviour of the power-law fluid is defined using Eq. (9) where \$K = 5 \times 10^{-3} \text{ Pa}\cdot\text{s}^n\$, with \$n = 0.652\$, and the interfacial surface tension is varied in the range \$10^{-7}\$–\$10^{-3} \text{ N/m}\$ to obtain different modified capillary numbers \$Ca\_p\$ in the range 0.06–0.8. The modified capillary number for the power-law fluid is defined according to Hewson et al. (2009) as:

$$Ca_p = \frac{K u_b^n}{0.5 w \sigma^{n-1}}; \text{ where } w \text{ is the channel - width} \quad (10)$$

Fig. 4(d) shows the comparison of the predicted value of the dimensionless liquid film thickness against the experimental values from Kamisli and Ryan (1999) and computational results from Hewson et al. (2009), for different modified capillary numbers. The actual bubble shape obtained from the present simulation and the asymptotic (analogous) liquid film thickness from Kamisli and Ryan (1999) are shown in Fig. 4(e) for a representative \$Ca\_p = 0.473\$. It is seen from the figures that the predictions are in good agreement with the literature for the entire range of capillary numbers considered, and the predicted bubble diameter (\$w - 2 \times t\_{\text{film}}\$) is within 2% of the experimental value (Kamisli and Ryan, 1999); this corresponds to a deviation of less than 5% in the dimensionless film thickness.

As mentioned in section ‘Problem description, geometry and computational domain’ of this paper, while all the simulations involving elongated Taylor bubbles are performed using an

axisymmetric mesh, those involving nearly spherical bubbles are performed using a full 3D mesh. Hence, to ensure consistency in the computational results reported in this paper, an exercise is carried out to compare the predicted bubble shape and velocities obtained using 2D axisymmetric and 3D simulations for cases involving Taylor bubbles. Fig. 5 illustrates the shapes of an elongated Taylor bubble obtained from the two meshes (axisymmetric and 3D) for a representative case; the operating condition corresponds to a bubble with  $d_e = 1.6$  cm rising in a circular tube with  $d = 0.96$  cm filled with water (Maeda, 1975). It is seen from the figure that the predicted bubble shapes are in excellent agreement with each other, thus reinforcing the validity of the present computational approach. The predicted bubble rise velocities for the case using the 2D axisymmetric and 3D meshes were within  $\pm 3.5\%$  of each other.

#### Dynamics of rising bubble in steady and pulsatile flow of water (Newtonian flow)

As indicated in Table 2, the effect of flow pulsations on the dynamics of a rising bubble in water is studied for bubble (equivalent) diameters  $d_e = 2, 6$  and  $10$  mm, dimensionless pulsation amplitude  $A = 0$  (steady),  $0.25, 0.5$  and  $1$ , and frequencies  $f = 0$  (steady),  $5$  and  $10$  Hz, for a mean liquid velocity  $u_l = 0.1046$  m/s (corresponding to  $Re = 600$ ) in a cylindrical tube of diameter  $d = 5$  mm.

Simulations with an entrapped bubble in steady liquid flow are performed to enable the isolation of the effects of pulsation on the dynamics of a rising bubble. Fig. 6 illustrates the variation in the velocity of an air bubble rising in a circular tube ( $d = 5$  mm), with water flowing co-currently at  $Re = 600$ . It is seen from the figure that for the range of bubble diameters considered, the velocity of the air bubble decreases with an increase in bubble size (or  $d_e$ ), and remains invariant for bubble diameters greater than the diameter of the tube. This is due to the fact that the influence of buoyancy (against drag inside the tube) is relatively greater for smaller bubbles, while the velocities of larger elongated bubbles that occur for bubble diameter greater than the diameter of the tube are determined by the average liquid velocity in the tube. Several studies (Maeda, 1975; Quan, 2011; Nicklin et al., 1962) have pointed out the rise velocity of Taylor bubbles in flowing liquid can be quantified as a linear combination of the co-current liquid velocity and the rise velocity of the bubble in a stagnant liquid as:

$$u_b = k_1 u_l + u_{b,s} + k_2 \quad (11)$$

where  $k_1$  and  $k_2$  are constants and  $u_{b,s}$  is the bubble rise velocity in a tube with stagnant fluid. Under conditions where a large bubble does not rise in the tube with stagnant liquid,  $u_{b,s} = 0$ , and  $k_2$  takes a negative value that depends on the tube diameter (Maeda, 1975), while for conditions where the bubble rises freely in a stagnant liquid,  $k_2 = 0$ . It is also seen from the Fig. 6 that the terminal velocity of the Taylor bubbles ( $d_e = 6, 10$  mm) obtained from the present simulations correlate very well against Maeda (1975), where,  $k_1 = 1.19$ ,  $k_2 = -0.0055$  m/s, with an error <1%.

Fig. 7 shows the transient evolution of bubble rise velocity for different bubble sizes ( $d_e = 2, 6, 10$  mm) under the same operating conditions as described for Fig. 6. While it is seen that the Taylor bubbles ( $d_e = 6, 10$  mm) reach a steady terminal rise velocity, the smaller bubble ( $d_e = 2$  mm) exhibits an oscillating velocity, although with a constant time averaged velocity magnitude. This is observed from the simulations to be due to a helical motion exhibited by the bubble, as also reported by several studies in the literature (Uno and Kintner, 1956; Tomiyama et al., 2002; Karamanev, 2001). In addition, an oscillation in the shape of the bubble was also observed, which reflects in the transient evolution of the bubble's centre of mass, and thus in the bubble velocity. It is

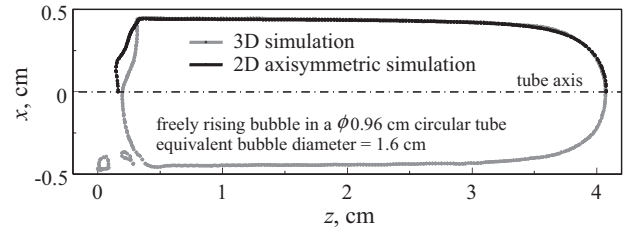


Fig. 5. Comparison of the bubble shapes obtained using 3D and 2D axisymmetric simulations.

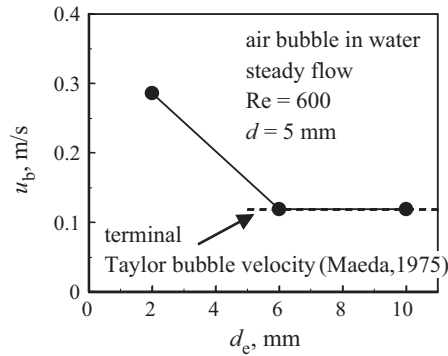


Fig. 6. Effect of bubble size on the velocity of an air bubble rising in a circular tube ( $d = 5$  mm), with steady flow of water at  $Re = 600$ .

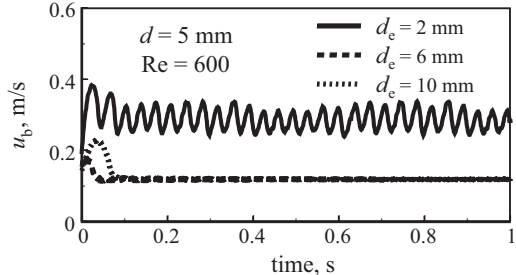
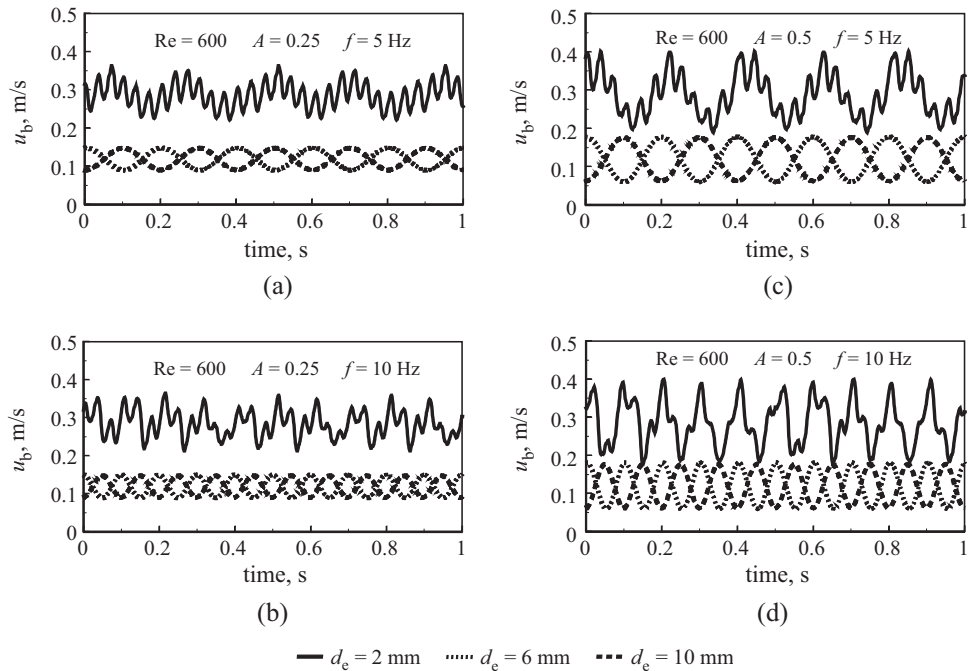


Fig. 7. Transient evolution of bubble rise velocity for different equivalent bubble diameters.

pointed out that the quantification of the aforementioned oscillation in bubble velocity is important to isolate the effect of pulsatile flow characteristics on the (oscillating) bubble velocity; this is discussed in the following section.

A comparison of the oscillating steady state velocities exhibited by the different sized bubbles moving in pulsatile flow of water, for a representative set of pulsation amplitudes  $A = 0.25, 0.5$ , and frequencies  $f = 5, 10$  Hz, is illustrated in Fig. 8(a)–(d). It is seen from the figures that irrespective of the amplitude or frequency of pulsation, the larger bubbles rise in the tube with a velocity that oscillates in-phase with the applied flow pulsations, while the smaller bubble ( $d_e = 2$  mm) seem to exhibit multiple frequencies in the oscillating rise velocity. It is also seen that similar to the steady flow conditions, the elongated bubbles with  $d_e = 6$  mm and  $10$  mm show identical oscillating characteristics in rise velocity during pulsatile flow. Recalling from the discussion presented in the preceding paragraph that the bubble with  $d_e = 2$  mm moves in helical path during steady co-current flow, the multiple frequencies exhibited by the bubble velocity as seen in Fig. 8(a)–(d) can be attributed to the direct consequence of the bubble exhibiting a similar motion during pulsatile flow conditions. It is seen from



**Fig. 8.** Comparison of transient oscillating bubble velocities between different sized bubbles, during bubble rise in a co-current pulsatile flow of water.

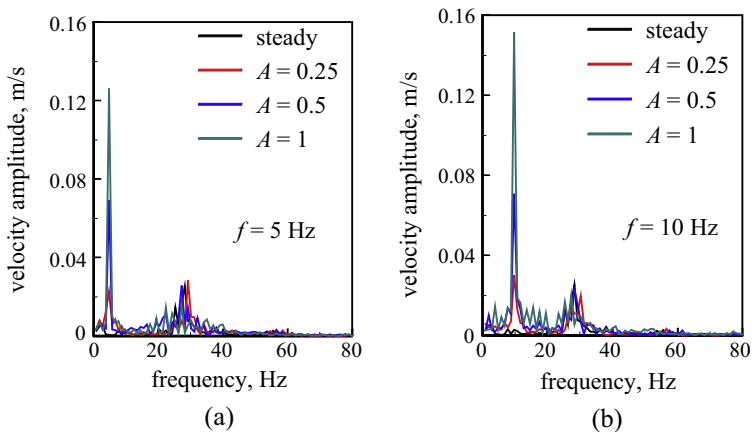


**Fig. 9.** Frequency distribution of the oscillating steady state bubble rise velocity for  $d_e = 2$  mm.

the discrete Fourier transform of the oscillating steady state velocity for  $d_e = 2$  mm, shown in Fig. 9, that the secondary frequency (i.e. other than the frequency of the pulsatile flow) is nearly 30 Hz, and invariant with any change in the applied amplitude of frequency of the pulsatile flow. It is also seen that, while the secondary frequency remains nearly unchanged with any variation in pulsatile flow characteristics, the amplitude of the bubble velocity pertaining to the secondary frequency reduces marginally for a prescribed change in  $f$  from 5 Hz to 10 Hz. It is also interesting to note that the amplitude of bubble velocity (for the primary frequency) increases slightly with an increase in pulsation frequency. This observation is evident from Fig. 10, where the effect velocity amplitudes obtained from Fourier transforms are compared for four pulsation frequencies (0, 5, 10, 30 and 40 Hz); note that  $f = 30$  Hz corresponds to a pulsation frequency equal to the secondary frequency in the bubble velocity due to its helical.

**Fig. 11(a)-(d)** illustrates the effect of pulsatile flow frequency and amplitude, respectively, on the oscillating steady state bubble

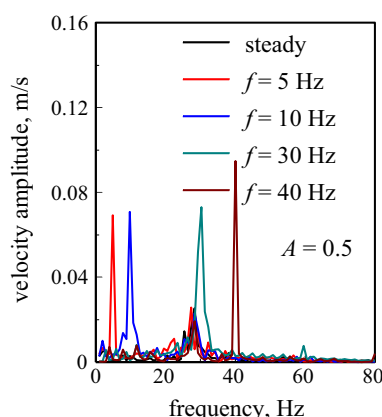


**Fig. 10.** Effect of the frequency of pulsatile flow on the frequency distribution of the oscillating steady state bubble rise velocity for  $d = 2$  mm.

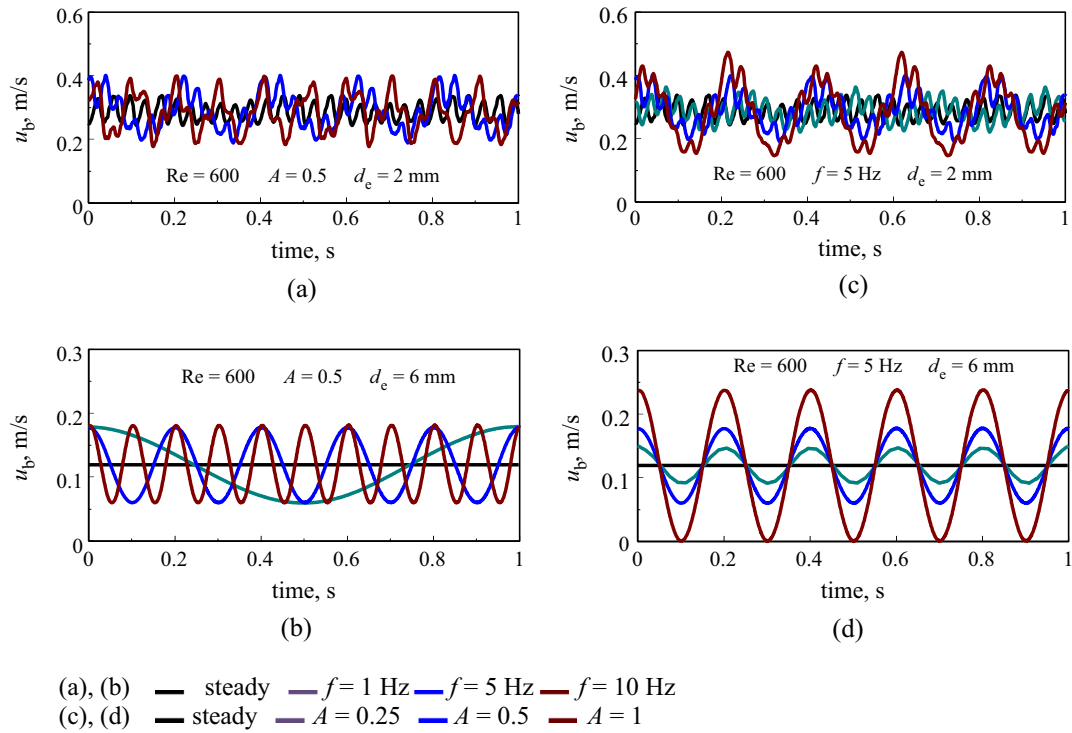


**Fig. 11.** Effect of pulsatile flow velocity frequency (a and b), and amplitude (c and d) on the dynamic steady state oscillations in bubble velocity.

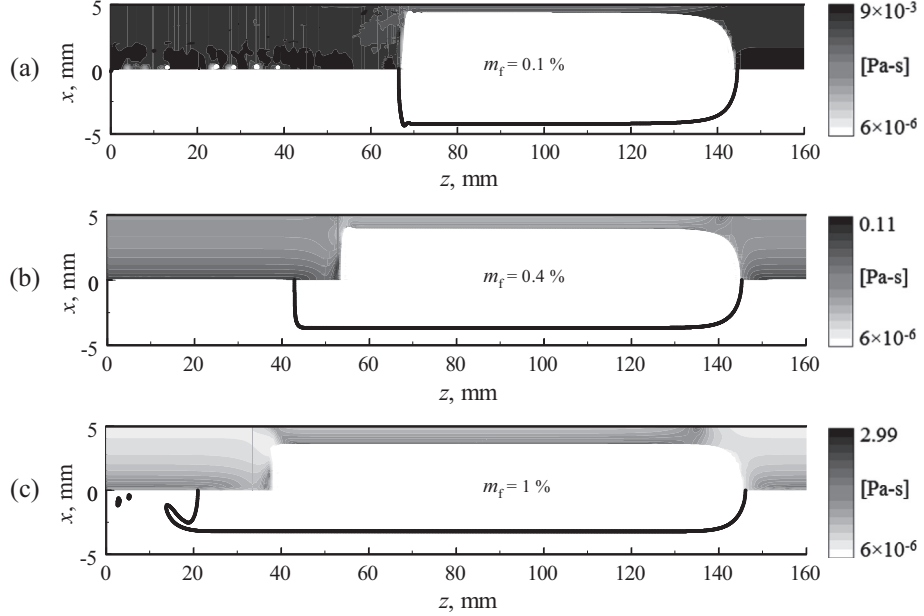
velocities for  $d_e = 2$  and 6 mm. Data for  $d_e = 10$  mm is not shown for brevity, as the qualitative trends are same as that obtained for  $d_e = 6$  mm. It is seen from the figures that while there is a concomitant variation in the oscillating amplitude and frequency of bubble velocity for any change in  $f$  or  $A$  over the range considered, there is no marked influence on the time-averaged bubble velocity. It was also observed that for the range of bubble diameters, pulsation amplitudes and frequencies explored in the present work with water as the liquid phase, the bubbles remained intact, and pulsations did not result in any bubble breakup.

#### Effect of shear-thinning liquid rheology on the dynamics of single Taylor bubble in steady co-current flow

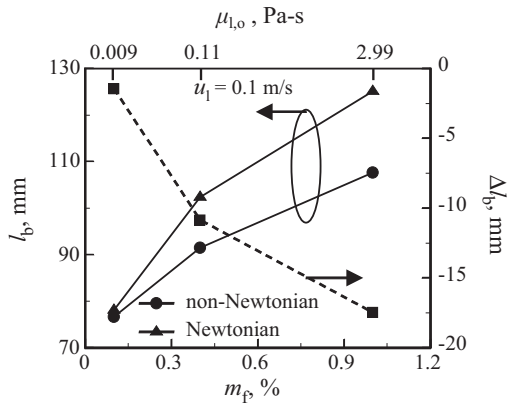
As indicated in Table 2, the effect of shear thinning behaviour during steady co-current flow is studied for bubble diameters  $d_e = 10$  and 20 mm, mean liquid velocity  $u_l = 0.1$  and 0.4 m/s, mass fraction of CMC in solution  $m_f = 0.1\%$ , 0.4% and 1%, in a cylindrical tube of diameter  $d = 10$  mm.

Fig. 12(a)–(c) shows the comparison between the bubble shapes obtained using Newtonian and shear-thinning treatment for the liquid viscosity, for  $m_f = 0.1\%$ , 0.4% and 1%, and for a representative set of other controlling parameters,  $u_l = 0.1$  m/s,  $d_e = 2$  cm and  $d = 1$  cm. The contours shown in the top-half of the figures indicate the variation in the liquid phase dynamic viscosity (due to shear-thinning), while the bottom-half of the figures show the corresponding bubble shapes obtained using a Newtonian treatment for the liquid viscosity, where a constant dynamic viscosity same as the zero-shear viscosity is prescribed, based on  $m_f$  (see Table 1). It is evident from the figures that an increase in  $m_f$  (or increase in the liquid phase dynamic viscosity) results in a concomitant increase in the length of the Taylor bubble, under both Newtonian as well as non-Newtonian conditions. As a consequence, the liquid film thickness (between the bubble–liquid interface and the tube wall) also increases with an increase in the  $m_f$ . In a recent Quan (2011) pointed out that an increase in the liquid

viscosity increases the viscous drag on the rising bubble, thereby tending to elongate the bubble. In a similar experimental work, study, Kajero et al. (2012) indicated that the relative elongation of the bubble with increase in liquid viscosity may be characteristic to flow inside tubes, and that the relative elongation with increase in viscosity will be pronounced for smaller tube diameters. A comparison of the lengths of the Taylor bubbles ( $l_b$ ) obtained from using Newtonian and non-Newtonian treatment of the liquid viscosity is shown in Fig. 13, for controlling parameters same as that shown in Fig. 12(a)–(c). It is seen from Figs. 12(a)–(c) and 13 that, while the length of the Taylor bubbles increases with an increase in  $m_f$  under both Newtonian and shear-thinning conditions, the length of the bubble is consistently longer when the liquid is treated as a Newtonian fluid. It is also seen from the Fig. 13 that the difference between the lengths of the bubbles obtained using the Newtonian and non-Newtonian treatments increases with an increase in mass fraction of CMC in the solution. This is due to the fact that, under non-Newtonian conditions, the effective dynamic viscosity of the liquid is lesser than  $\mu_{l,o}$  in the tube due to the liquid-shear with the tube walls (as the CMC solution is a shear-thinning liquid). Hence, in line with the preceding discussion, that the bubble length increases with an increase in liquid viscosity, the reduction in the viscosity (and hence, the drag) due to shear under non-Newtonian conditions results in consistently shorter Taylor bubbles under shear-thinning conditions. In coherence, as the effect of shear in the liquid film around the bubble on the reduction of viscosity increases with an increase in the mass fraction of CMC (see Table 1: the dynamic viscosity reduces by about one order of magnitude for  $m_f = 0.1\%$ , while more than three orders of magnitude for  $m_f = 1\%$ , over the range of strain rates), the reduction in the effective viscosity is relatively higher for higher values of  $m_f$  due to the rheological characteristics of the fluid. Thus, a greater difference in the bubble lengths is observed for relatively higher values of  $m_f$  as seen in the figure. This is corroborated by the variation in the ratio of non-Newtonian liquid viscosity to the zero-shear viscosity along the inlet of the tube



**Fig. 12.** Dynamic viscosity distribution (shown only for non-Newtonian cases) around the bubble and bubble shape for different CMC mass fractions, for  $u_l = 0.1 \text{ m/s}$ ,  $d_e = 2 \text{ cm}$ ,  $d = 1 \text{ cm}$ . Note: the top-half of figures correspond to shear-thinning treatment of the liquid viscosity, and the bottom-half of the figures correspond to the Newtonian treatment of the liquid.



**Fig. 13.** Comparison of the lengths of the Taylor bubbles obtained from in Newtonian and shear-thinning liquids for  $u_l = 0.1 \text{ m/s}$ ,  $d_e = 2 \text{ cm}$  and  $d = 1 \text{ cm}$ ;  $\Delta l_b = l_{b,\text{non-Newtonian}} - l_{b,\text{Newtonian}}$ .

(under fully developed flow) shown in Fig. 14. The variation in the dynamic viscosity between the tube-axis and the tube-walls increases from about 10% for  $m_f = 0.1\%$  and  $u_l = 0.1 \text{ m/s}$  (and about 20% for  $u_l = 0.4 \text{ m/s}$ ) to about 90% for  $m_f = 1\%$  (and 95% for  $u_l = 0.4\%$ ), *ceteris paribus*.

As the present study deals with upward (co-current) liquid flow, buoyancy force as well as the pressure gradient in the tube synergistically aid bubble rise, due to which, the bubble velocity is greater than the mean liquid velocity. As the bubble progresses in the liquid, the surrounding liquid is pushed around the bubble from the nose to the tail resulting in a flow field similar to a pressure-driven Poiseuille flow (in the direction opposite to bubble rise) in the liquid layer adjacent to the elongated section of the Taylor bubble (Quan, 2011; Nogueira et al., 2005). The fully developed flow in the liquid film can be seen from the velocity profiles shown in Fig. 15 for a representative case. Fig. 16 illustrates the variation in this fully developed liquid velocity in the liquid film for different values of  $m_f = 0.1\%$ , 0.4% and 1%, obtained under Newtonian and shear-thinning conditions, for  $u_l = 0.1 \text{ m/s}$ ,

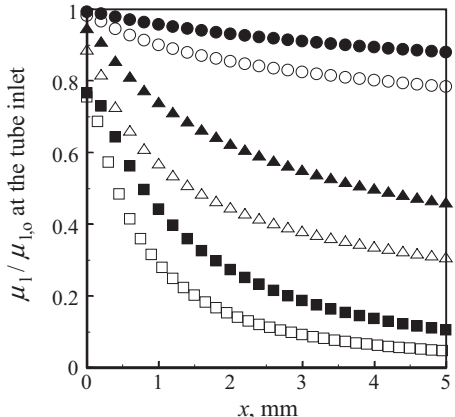


**Fig. 14.** Distribution of the ratio of shear-thinning dynamic viscosity to the zero-shear dynamic viscosity dynamic across the inlet of the tube for different values of  $m_f$  and  $u_l$ .

$d_e = 2 \text{ cm}$  and  $d = 1 \text{ cm}$ . It is seen from the figure that the velocity in the liquid film reduces with an increase in  $m_f$  (or implicitly, the dynamic viscosity) under both Newtonian and non-Newtonian conditions, due to the thicker liquid film obtained under higher values of  $m_f$  (see Fig. 12). For the largest mass fraction of CMC (1%) considered in the present study, the liquid film velocity is almost zero under both Newtonian and non-Newtonian conditions, as seen in the figure. The manifestation of the relatively low liquid flow rate in the liquid film, indicative of a low liquid strain rate in region, is seen as the higher values of dynamic viscosity in the liquid film in the contours illustrated in Fig. 12(c). It is also seen that the liquid velocity under non-Newtonian conditions is consistently higher than under Newtonian treatment for any

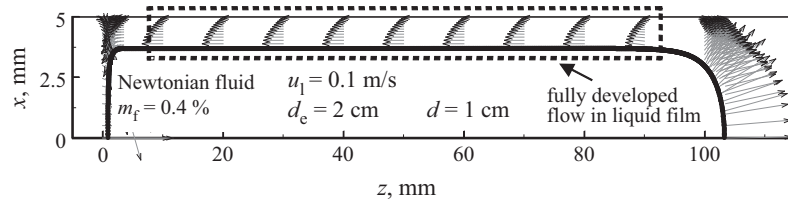


**Fig. 15.** Velocity vectors in the liquid around the bubble obtained during the rise of a Taylor bubble in co-current flow of Newtonian fluid.

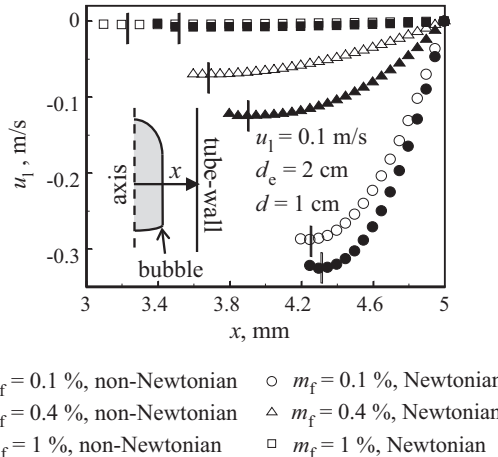


**Fig. 16.** Comparison of the velocity distribution in the fully developed liquid film around the Taylor bubble obtained in Newtonian and shear thinning liquids for different values of  $m_f$ .

given value of the  $m_f$ . This can be attributed to the direct consequence of the shear induced reduction in the dynamic viscosity of the liquid under non-Newtonian conditions, as outlined in the preceding paragraph (discussion on Fig. 14). It is also seen from Fig. 16 that the difference in the velocity at the liquid–bubble interface (indicated with a line in the figure) between the Newtonian and non-Newtonian conditions increases with an increase in  $m_f = 0.1\text{--}0.4\%$ , but subsequently decreases for  $m_f = 1\%$ .

Fig. 17 shows the variation in the terminal velocity of the bubble with change in CMC mass fraction for different equivalent bubble diameters  $d_e = 1, 2 \text{ cm}$ , and mean liquid velocities  $u_l = 0.1, 4 \text{ m/s}$ , obtained under Newtonian and non-Newtonian conditions.

It is seen from the figures that the velocities of the bubbles with both  $d_e = 1 \text{ cm}$  and  $2 \text{ cm}$ , are equivalent, irrespective of other controlling parameters. While this was already noted in the discussion presented in the previous section of this paper on Taylor bubbles moving through water, the same appears to hold good under non-Newtonian conditions as seen in Fig. 17. It is also seen from the figure that for the Newtonian conditions, the bubble velocity increases with an increase in mass fraction for the range of parameters considered. This can be attributed to the fact that, while the buoyancy force is the same for all values of  $m_f$  due to a negligible change in the liquid density over the range of  $m_f$  considered, the pressure difference across the tube to drive the liquid at the velocity  $u_l$  increases with an increase in  $m_f$  (due to the concordant increase in dynamic viscosity), thus aiding in the upward movement of the bubble. In addition, the reduction in the cross-sectional diameter of the bubble for a greater  $m_f$  (see Fig. 12), results in a reduced pressure drag force on the bubble (Nogueira et al., 2005). This is contrary to what happens during the rise of Taylor bubbles in stagnant fluids where the rise velocity decreases with an increase in liquid viscosity (Nogueira et al., 2005; Sousa et al. 2005). This is because, unlike co-current flow where the pressure difference across the tube increases with an increase in liquid viscosity (or  $m_f$ ) for any given value of  $u_l$ , the hydrodynamic head remains the same with any change in  $m_f$  during bubble rise in a stagnant column of liquid due to a negligible change in liquid density with change in  $m_f$ . It is however seen that the degree to which the bubble velocity increases with increase in mass fraction is lower between  $m_f = 0.4\%$  and  $1\%$  as compared to  $m_f = 0.1\%$  and  $0.4\%$ , due to the greater influence of the shear drag on the bubble for higher viscosities (or  $m_f$ ). In line with this discussion, and considering that the dynamic viscosity of the liquid in the tube under non-Newtonian conditions is lower than that under Newtonian conditions, the bubble rise velocity under the former are consistently relatively lower, irrespective of other controlling

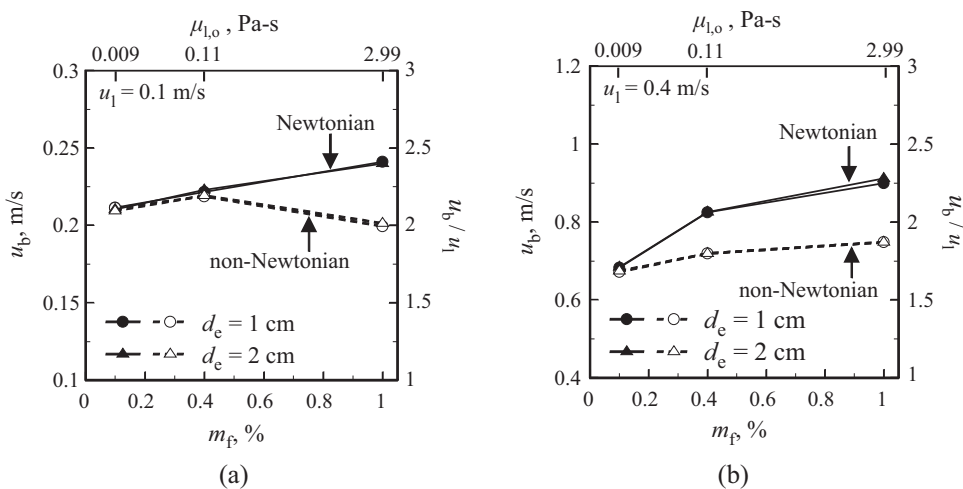


**Fig. 17.** Change in the terminal velocity of the bubble with change in CMC mass fraction for different equivalent bubble diameters and mean liquid velocities.

parameters. Besides, as shown in the representative case in Fig. 18 ( $u_l = 0.1 \text{ m/s}$ ,  $d_e = 1 \text{ cm}$ ,  $d = 1 \text{ cm}$ ,  $m_f = 0.4\%$ ), the sharper nose of the bubble obtained during the Newtonian condition results in a lower drag force on the bubble as compared to the relatively blunt nose observed in the non-Newtonian condition, thereby resulting in a higher bubble velocity during the Newtonian condition. It is also seen that the bubble velocity reduces, although marginally, between  $m_f = 0.4\%$  and 1%, under the non-Newtonian treatment, for  $u_l = 0.1 \text{ m/s}$ , indicating that an optimum value of  $m_f$  may exist for any given value of the mean co-current liquid velocity for a maximum bubble velocity (or least drag). For any given value of  $m_f$ , as the liquid viscosity in the tube is relatively greater for  $u_l = 0.1 \text{ m/s}$  as compared to  $u_l = 0.4 \text{ m/s}$  (see Fig. 14), it is possible that the optimum value of  $m_f$  for  $u_l = 0.4 \text{ m/s}$  is greater than that for  $u_l = 0.1 \text{ m/s}$ ; not obtained under the range of parameters considered. It is also seen from Fig. 19 that the curvature at the bubble nose is greater for  $u_l = 0.4 \text{ m/s}$  as compared to  $u_l = 0.1 \text{ m/s}$  irrespective of the bubble size. The results for the corresponding Newtonian cases are similar, and hence omitted for brevity. The sharper nose of the bubble results in reduced pressure drag on the bubble at higher velocities. It is inferred from Figs. 19 and 12(a)–(c), that both, the co-current flow velocity as well as the liquid viscosity affects the bubble shape. It was

reported in Quan (2011) that the assumption of dimensional similarity for the bubble shapes as presented in Dumitrescu (1943) is not entirely accurate, and the liquid viscosity affected the bubble shape of the Taylor bubbles, particularly during co-current flows. In addition, the computational simulations carried out in the present research have shed light on the effects of non-Newtonian viscosity variation on the bubble shape and dynamics under different co-current flow conditions.

#### Dynamics of a single Taylor bubble in pulsatile co-current flow of shear-thinning liquid

As indicated in Table 2, the effect of flow pulsations on the dynamics of a rising Taylor bubble in non-Newtonian fluid co-current flow is studied for  $d_e = 20 \text{ mm}$ ,  $u_l = 0.1$  and  $0.4 \text{ m/s}$ ,  $m_f = 0.1$ , and 1%, in a cylindrical tube with  $d = 10 \text{ mm}$ .

Figs. 20(a)–(h) and 21(a)–(h) show the shape and progression (over a cycle of pulsation) of a rising Taylor bubble during pulsatile co-current flow for  $m_f = 0.1\%$  and 1%, respectively, and for  $u_l = 0.1 - \text{m/s}$ ,  $f = 5 \text{ Hz}$  and  $A = 1$ . It is seen from the figures that, as observed during steady co-current flow conditions, the length of the bubble is consistently longer for  $m_f = 1\%$  as compared to  $m_f = 0.1\%$  even during pulsatile flow. It is also seen that the length of the bubble does not vary significantly during the cycle of pulsation for both cases; the calculated variation in the bubble length over a cycle of pulsation is <0.9%. It is interesting to note that while the qualitative shape of a Taylor bubble for  $m_f = 0.1\%$  is the same as that observed during steady flow conditions, there exists a distinct waviness (ripple) in the shape, particularly in the elongated region of the bubble, for  $m_f = 1\%$ . The wavelength of the ripple on the body of the Taylor bubble is about 45 mm for the case shown in the figure for  $m_f = 1\%$ . It is also seen from the Fig. 21(a)–(h) that the locations of the ripple with reference to the tube-wall stays constant over the cycle, thus resulting in standing wave, as the bubble progresses upward through the tube. This would imply that the ripples on the bubble's body move in a direction opposite to the bubble and at the same velocity as the bubble's rise velocity, which is unlike the capillary waves that generally progress upward from the tail of the bubble. Liberzon et al. (2006) showed that the capillary waves are primarily induced on the liquid–bubble interface due to the oscillations in the tail of the bubble and propagate upwards, depending on the wave-current interactions along the liquid film. Fig. 22(a)–(h) shows the shape and progression of the bubble for  $f = 10 \text{ Hz}$ , and other parameters same as those mentioned for Fig. 21(a)–(h). From a comparison of the two aforementioned figures with  $m_f = 1\%$ , it is seen that the number of ripples on

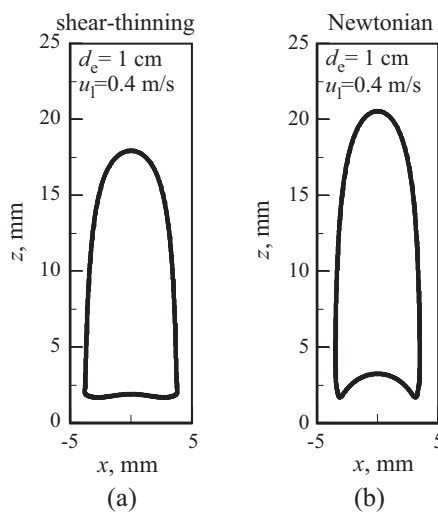


**Fig. 18.** Comparison of bubble shape obtained during bubble rise in Newtonian and shear-thinning liquids;  $m_f = 0.4\%$ .

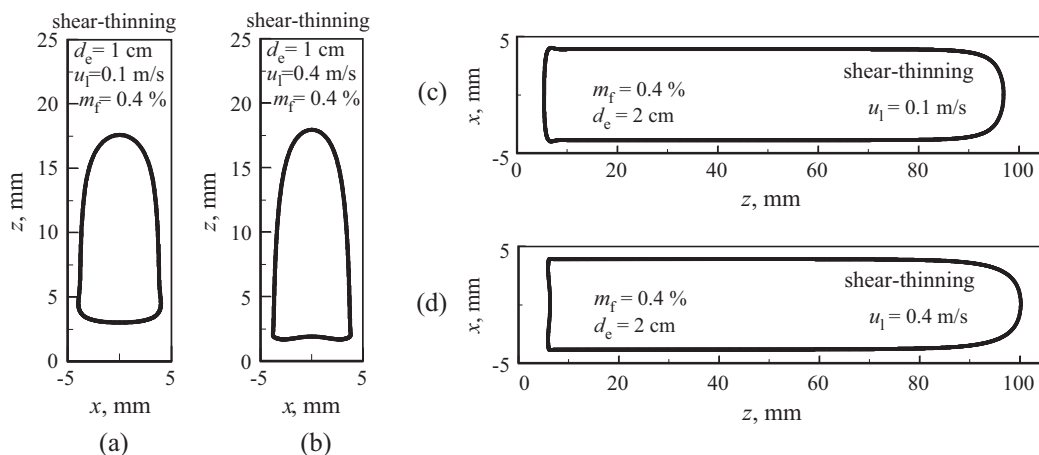


**Fig. 19.** Comparison of bubble shapes in between two different co-current liquid (shear-thinning) velocities.

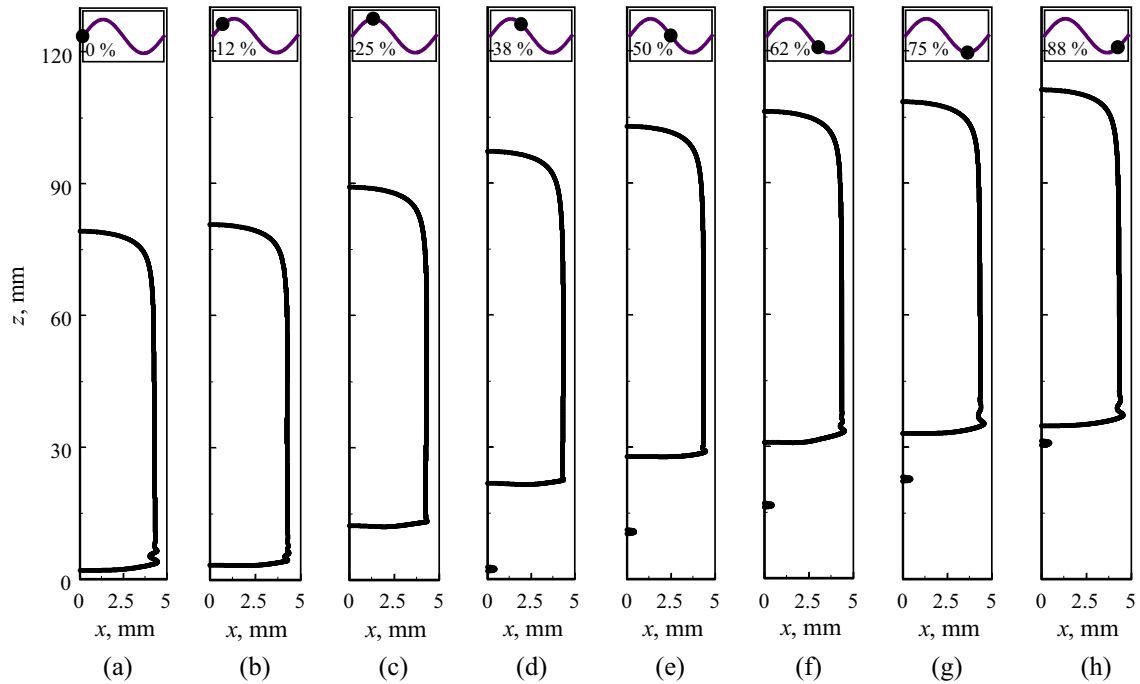


**Fig. 20.** Progression of a rising Taylor bubble in pulsatile co-current flow of shear-thinning fluid over a cycle of pulsation, for  $m_f = 0.1\%$ ,  $u_l = 0.1 \text{ m/s}$ ,  $f = 5 \text{ Hz}$ ,  $A = 1$ , and  $d_e = 2 \text{ cm}$ .

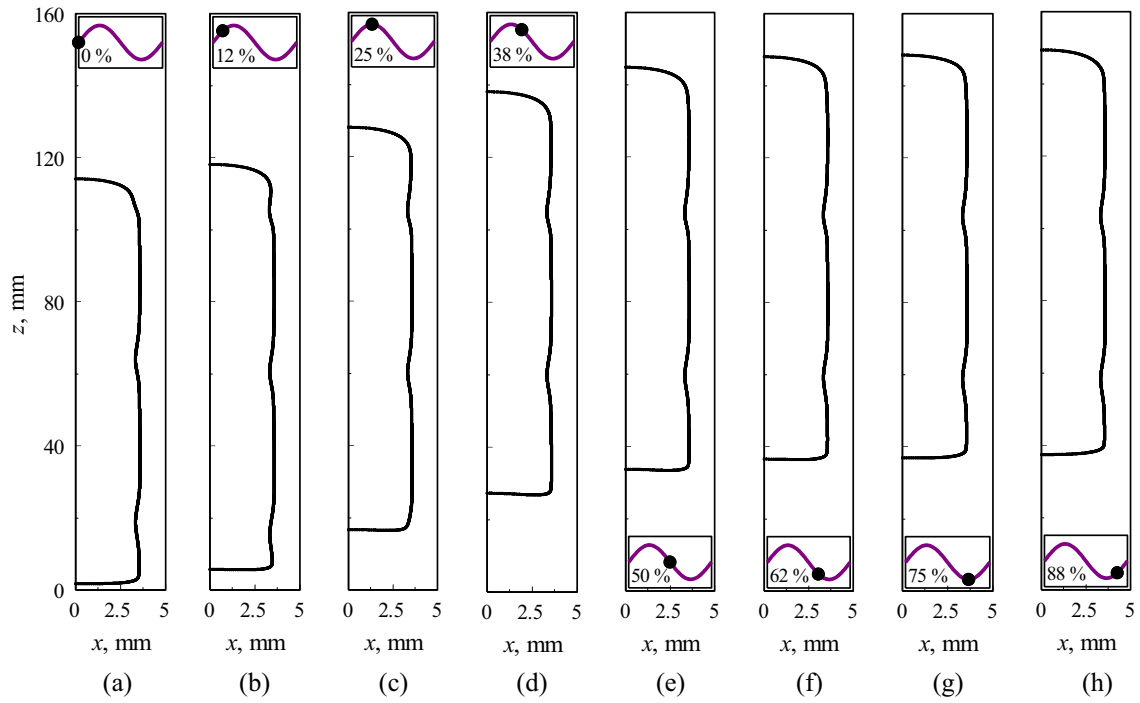


**Fig. 21.** Progression of a rising Taylor bubble in pulsatile co-current flow of shear-thinning fluid over a cycle of pulsation, for  $m_f = 1\%$ ,  $u_l = 0.1 \text{ m/s}$ ,  $f = 5 \text{ Hz}$ ,  $A = 1$ , and  $d_e = 2 \text{ cm}$ .

the bubble increases with the frequency of the pulsatile flow. Interestingly, the wavelength of the ripples decreases proportionally with the frequency of co-current flow pulsation. The calculated wavelength of the ripple for  $f = 10 \text{ Hz}$  was 22.5 mm, while that for  $f = 5 \text{ Hz}$ , *ceteris paribus*, is 45 mm. It is also seen from the figures that the amplitude of the ripple on the body of the bubble remains nearly the same for the two frequencies considered, irrespective of the location of the ripples on the bubble. It is seen from a

comparison of the bubble shapes between  $A = 0.5$  and 1 ( $u_l = 0.1 \text{ m/s}$ ,  $m_f = 1\%$ ,  $f = 10 \text{ Hz}$ ) shown in Fig. 23(a) and (b) that the amplitude (and also the peak-to-valley distance) of the ripple on the body of the bubble decreases with a decrease in amplitude of co-current flow pulsation. The peak to valley length on the ripple (in the fully developed liquid film region) for the cases shown in Fig. 23(a) and (b) is found to be about 0.15 mm for  $A = 0.5$  and about 0.26 mm for  $A = 1$ .

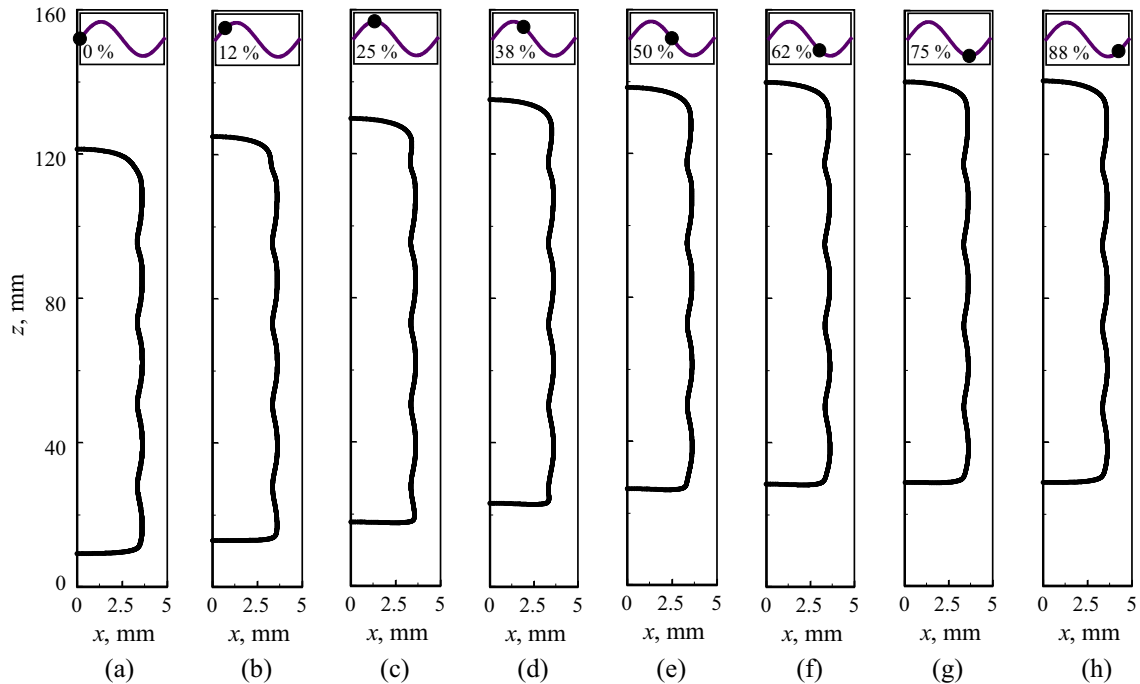


**Fig. 22.** Progression of a rising Taylor bubble in pulsatile co-current flow of shear-thinning fluid over a cycle of pulsation, for  $m_f = 1\%$ ,  $u_l = 0.1 \text{ m/s}$ ,  $f = 10 \text{ Hz}$ ,  $A = 1$ , and  $d_e = 2 \text{ cm}$ .

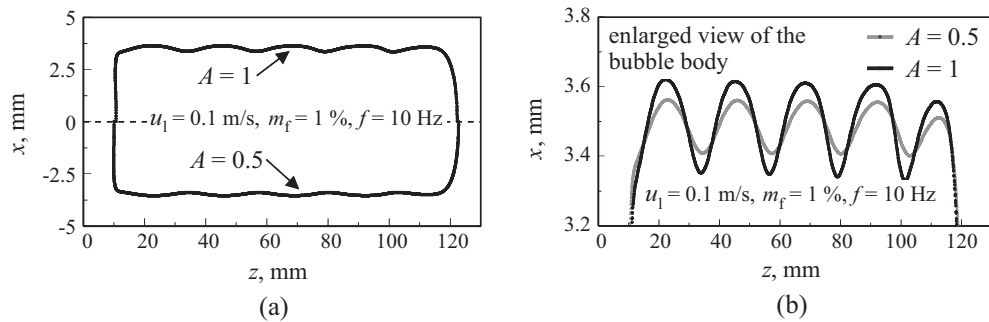


**Fig. 23.** Comparison of bubble shapes obtained for different pulsatile flow amplitudes, for  $m_f = 1\%$ ,  $u_l = 0.1 \text{ m/s}$  and  $f = 10 \text{ Hz}$ .

The velocity inside and around the bubble for  $m_f = 0.1\%$  and  $m_f = 1\%$  for a representative set of other controlling parameters is illustrated in Fig. 24(a) and (b). It is seen that while for  $m_f = 0.1\%$ , the re-circulation region inside the bubble extends to the full length of the bubble (as is the case for any rising Taylor bubble in steady co-current flow (Quan, 2011)), there are individual re-circulation regions near each ripple for the case with  $m_f = 1\%$ ; note that only one such section of the bubble is shown in Fig. 24(b) for an enhanced view of the local flow field. It is also seen from the dynamic viscosity contours shown in Fig. 24(b) that the local dynamic viscosity in the region of the ripple is relatively higher than the regions upstream and downstream. The localised region of high viscosity results in a greater drag on the bubble in the vicinity. From the linear relationship between the frequency of pulsation and the number of ripples found on the bubble outlined earlier, it is understood that the standing wave (in the tube) plays a direct role in determining the number of ripples, or in influencing the spacing between the locations of the tube that potentially result in ripples on the bubble. Besides, the proportional change in the size of the ripple with change in amplitude of pulsation also suggests a strong relationship between the imposed fluid pulsations on the formation of ripples on the surface. Hence, it is

understood that the complex interplay between the variations in viscosity due to the standing waves generated in the tube at specific locations (based on the frequency) and magnitude (based on amplitude), along with the large film thickness that are obtained for relative high viscosities (as discussed in section ‘Effect of shear-thinning liquid rheology on the dynamics of single Taylor bubble in steady co-current flow’) eventually lead to several recirculation cells inside the bubble due to a localised increase in drag on the bubble, along with ripples on the bubble–liquid interface. An additional simulation was carried out for  $f = 10 \text{ Hz}$ ,  $A = 1$  and  $u_l = 0.1 \text{ m/s}$  by assuming the fluid to be Newtonian (with  $m_f = 0.4\%$ ) to isolate the effects of non-Newtonian viscosity variation on the formation of the ripples on the Taylor bubble. Fig. 25 illustrates the corresponding bubble shape and streamlines inside and around the bubble for the aforementioned case. It is seen that, similar to the observation in the non-Newtonian cases discussed earlier, individual recirculation cells inside the bubble are also observed in the Newtonian fluid, along with waviness of the bubble surface. However, the shape and structure of this waviness are irregular in comparison to non-Newtonian cases discussed earlier. Hence, it is possible that as both, the liquid as well as the gas are incompressible (for the conditions assumed in the present

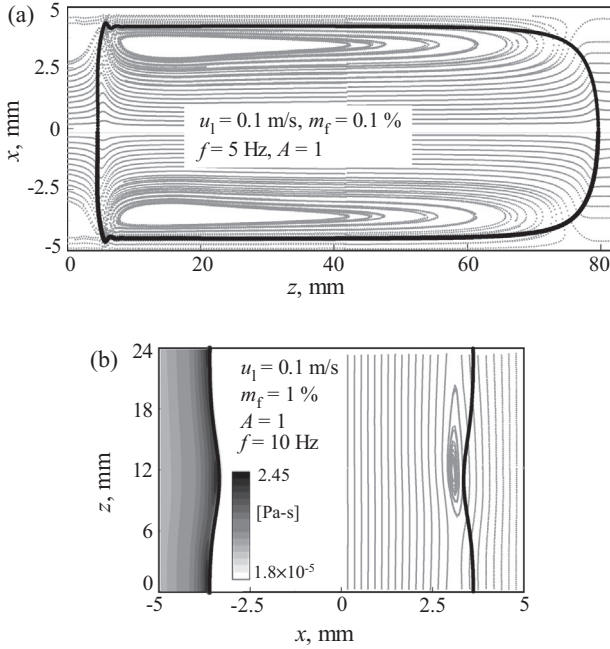


**Fig. 24.** Velocity streamlines inside and around (a) the entire bubble for  $m_f = 0.1\%$  and (b) in a section of a Taylor bubble for  $m_f = 1\%$ .

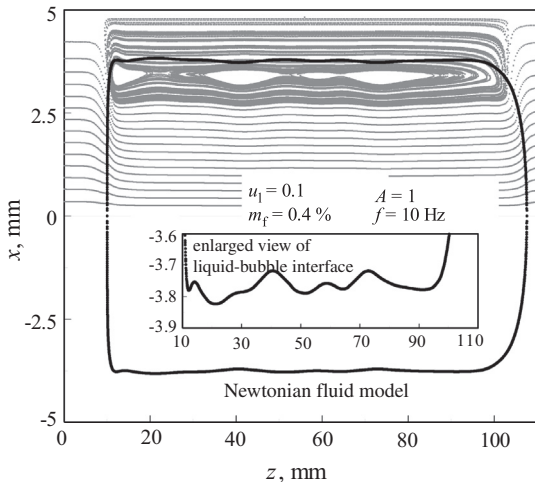


**Fig. 25.** Shape and velocity streamlines inside and around the bubble for  $m_f = 0.4\%$  (with Newtonian viscosity model),  $u_l = 0.1\%$ ,  $f = 10 \text{ Hz}$  and  $A = 1$ .

research), the viscosity variation in the non-Newtonian liquid work in tandem with the standing waves in the tube due to pulsatile flow (which seem to have a greater impact on the ripples), as compared to the Newtonian cases, to result in relatively more regular ripples on the bubble. Hence, the characteristics of the ripples on the Taylor bubble rising in co-current flow are dictated by the combined effect of the five factors: (i) characteristics of the pulsatile flow, (ii) surface tension of the liquid–gas combination, (iii) buoyancy, (iv) liquid viscosity, and (v) dimensions of the tube. Since such ripples are not observed under low liquid viscosities (Fig. 23(a)–(h)), the greater liquid film thickness that exists for relatively greater viscosities under both Newtonian as well as non-Newtonian conditions (Fig. 12) is able to better accommodate the oscillations on the liquid–bubble interface. A further investigation is required to characterise the ripples on the Taylor bubbles based on the five strongly influencing parameters identified in the present study.

Fig. 26 shows the variation in the bubble velocity, with change in the amplitude of pulsatile flow velocity, for different mass fractions of CMC ( $m_f = 0.1\%$  and  $1\%$ ), and for  $u_l = 0.1 \text{ m/s}$  and  $f = 10 \text{ Hz}$ . It is seen from the figures that, as expected, the amplitude of oscillating bubble velocity increases concomitantly with an increase in pulsatile flow amplitude, for both values of  $m_f$  shown. However, for any given amplitude of pulsatile flow, the amplitude of oscillating bubble velocity is consistently higher for  $m_f = 1\%$  as compared for  $m_f = 0.1\%$ . Extending this observation, and considering that the viscosity variation due to fluid shear for  $m_f = 0.1\%$  is significantly lower (making it behave more like a Newtonian fluid), it is evident that the bubble responds to pulsations in a non-Newtonian fluid relatively more than in a Newtonian fluid. The relative change in the bubble velocity with change in the liquid velocity under steady conditions as shown in Fig. 27 is also indicative that the change in bubble velocity with a change in liquid velocity (through a cycle of pulsation) is greater for relatively higher values of  $m_f$ . Fig. 28 shows the variation in bubble velocity with variation in pulsatile flow frequency for different values of  $m_f = 0.1\%$  and  $1\%$ , and for a representative case:  $u_l = 0.1 \text{ m/s}$  and  $A = 1$ . It is seen that unlike the influence of pulsatile flow amplitude, the effect of pulsatile flow frequency is negligible on the transient characteristics of the bubble velocity over the range of parameters considered, despite significant differences observed in the bubble shape with an increase in frequency. The bubble exhibits an oscillatory velocity with a frequency same as the applied pulsatile flow, and without any phase difference.

Fig. 29(a) and (b) shows the comparison of the transient oscillating bubble velocity and dimensionless bubble velocity with change in  $m_f$  for different mean pulsatile flow velocities  $u_l = 0.1$  and  $0.4 \text{ m/s}$ , and for representative values of  $f = 10 \text{ Hz}$  and  $A = 0.5$ . With a view to evaluate the effectiveness of flow pulsations

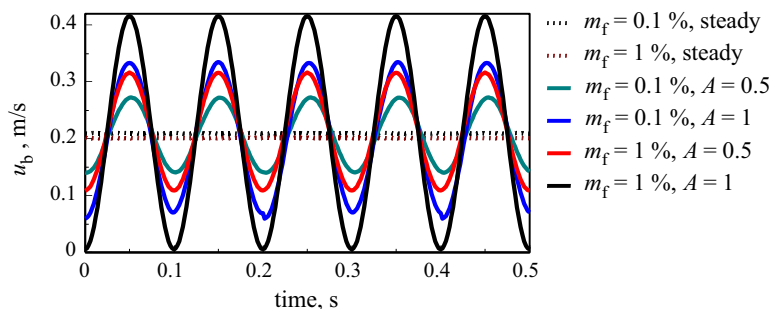


**Fig. 26.** Comparison of bubble velocity between  $m_f = 0.1\%$  and  $1\%$  for different co-current flow pulsating amplitudes, for  $u_l = 0.1 \text{ m/s}$  and  $f = 10 \text{ Hz}$ .

on the rise velocity of Taylor bubbles in a co-current flow of shear-thinning fluids, the dimensionless bubble velocity is defined as follows:

$$u_b^* = (u_{b,p} - u_{b,s})/u_{b,s} \quad (10)$$

where  $u_{b,p}$  and  $u_{b,s}$  are the bubble rise velocities under pulsatile and steady co-current flows, respectively. It is seen from the figures that the change in the amplitude of oscillating bubble velocity is greater for  $u_l = 0.1 \text{ m/s}$  as compared to  $u_l = 0.4 \text{ m/s}$ . This can be attributed to

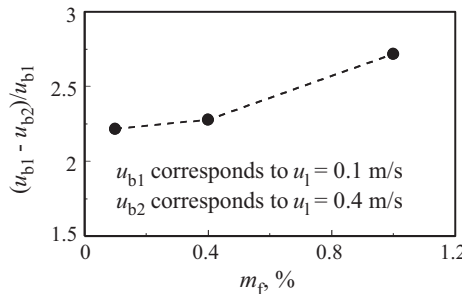


**Fig. 27.** Relative change in bubble velocity with change in mean steady liquid velocity for different values of  $m_f$ .

the fact that the relative change in the liquid viscosity with change in instantaneous liquid velocity over a cycle of pulsation is greater for  $u_l = 0.1 \text{ m/s}$  as compared to  $u_l = 0.4 \text{ m/s}$ . It was also observed in the simulations that under conditions of higher dimensionless pulsatile flow amplitudes (such as  $A = 1$  considered for the present study) and high co-current liquid velocity, irrespective of the value of pulsatile flow frequency over the range studied in the present research, the Taylor bubble disintegrated into smaller bubbles. Considering the inferences from Figs. 26, 27 and 29(a) and (b), the present study reveals that the dynamics of a Taylor bubble in pulsatile non-Newtonian flow is more susceptible to the amplitude than the frequency of co-current flow pulsations. It is also reasonable to assume that the introduction of flow pulsations with large amplitudes can be a viable technique to break the elongated Taylor bubbles in applications involving slug flows. However, it is pointed out that the behaviour and response of a stream of Taylor bubbles in continuous slug flows may be different from that observed in the present study with a single Taylor bubble. Hence a further investigation is required to characterise the conditions under which bubble breakup may occur for continuous slug flows. It is also pointed out that a complete 3-dimensional modeling of the flow domain may be required to capture bubble breakup to avoid unphysical bubble shapes (such as annular bubbles) that may be obtained under 2-dimensional axisymmetric conditions.

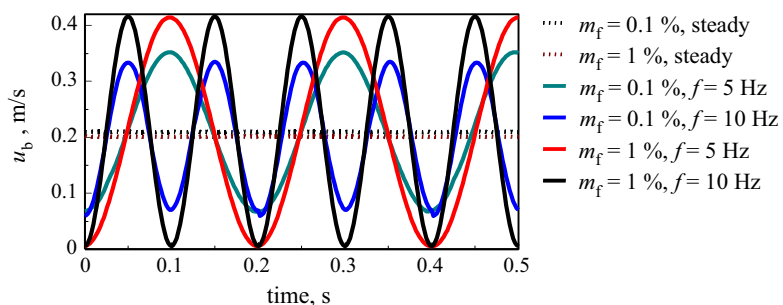


**Fig. 28.** Comparison of bubble velocity between  $m_f = 0.1\%$  and  $1\%$  for different co-current flow pulsating frequencies, for  $u_l = 0.1 \text{ m/s}$  and  $A = 1$ .

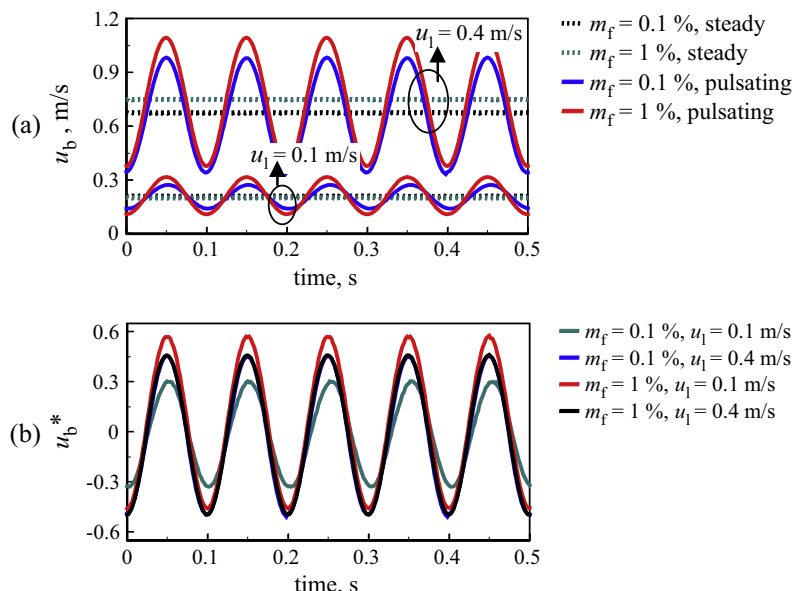


**Fig. 29.** Comparison of (a) bubble velocity and (b) dimensionless bubble velocity between  $m_f = 0.1\%$  and  $1\%$  for different co-current flow pulsating flow velocities (mean), for  $A = 0.5$ ,  $f = 10 \text{ Hz}$ .

## Conclusions

A computational analysis using the algebraic VOF approach available in OpenFOAM is carried out to determine the effects of co-current steady and pulsatile flow on the shape and rise velocity of a Taylor bubble in both Newtonian and shear-thinning non-Newtonian liquids with different viscous properties. The key conclusions derived from the present investigation are as follows:

- (i) Unlike the Taylor bubbles, the smallest bubble (with an equivalent diameter  $d_e = 0.2$  cm) exhibited an oscillatory helical motion under both steady as well as pulsatile co-current flow conditions. A secondary oscillatory frequency (i.e. other than the frequency of pulsatile co-current flow) is observed at approximately 30 Hz, irrespective of the amplitude or frequency of the co-current liquid velocity.
- (ii) The transient and time-averaged velocities of the elongated Taylor bubbles were equivalent under both steady as well as pulsatile co-current flows in the air–water system.
- (iii) In contrast to observations in stagnant liquid columns, an increase in the dynamic viscosity of the liquid (Newtonian) results in a concomitant increase in the bubble velocity for any given co-current liquid velocity; for shear-thinning non-Newtonian liquids, the change in the bubble velocity with an increase in  $m_f$  is comparatively greater at higher co-current velocities.
- (iv) During bubble rise in pulsatile flows of shear-thinning liquids, distinct ripples are found to occur on the bubble surface at higher values of  $m_f$ , the locations of which remained stationary with reference to the tube for any given pulsatile flow frequency. In contrast, capillary waves were found to occur on the Taylor bubble rising in high viscosity Newtonian liquids.
- (v) The amplitude and wavelength of the ripples varied proportionally with the amplitude and frequency of the co-current flow pulsation, respectively.
- (vi) The amplitude of the bubble velocity oscillations increase with an increase in the mass fraction of CMC in water for any given amplitude of pulsatile co-current flow; the effect of frequency on the rise velocity of the bubble was found to be weak for the range of parameters studied.
- (vii) For high amplitude and mean velocity of the pulsatile flow, the bubble was found to disintegrate into smaller bubbles.

## Acknowledgement

This work was supported by iVEC Pawsey Supercomputing Centre, Perth, Western Australia through the use of its advanced computing facility and resources.

## References

- Acharya, A., Ulbrecht, J.J., 1978. Note on the influence of viscoelasticity on the coalescence rate of bubbles and drops. *A.I.Ch.E. J.* 24, 348–351.
- Amirnia, S., de Bruyn, J.R., Bergougnou, M.A., Margaritis, A., 2013. Continuous rise velocity of air bubbles in non-Newtonian biopolymer solutions. *Chem. Eng. Sci.* 94, 60–68.
- Benchabane, A., Bekkour, K., 2008. Rheological properties of carboxymethyl cellulose (CMC) solutions. *Colloid Polym. Sci.* 286, 1173–1180.
- Brackbill, J.U., Kothe, D.B., Zemach, C., 1992. A continuum method for modeling surface tension. *J. Comput. Phys.* 100, 335–354.
- Brannock, D., Kubie, J., 1996. Velocity of long bubbles in oscillating vertical pipes. *Int. J. Multiph. Flow* 22 (5), 1031–1034.
- Carew, P.S., Thomas, N.H., Johnson, A.B., 1995. A physically based correlation for the effects of power law rheology and inclination on slug bubble rise velocity. *Int. J. Multiph. Flow* 21 (6), 1091–1106.
- Chhabra, R.P., Richardson, J.F., 1999. Non-Newtonian Flow in the Process Industries: Fundamentals and Engineering Applications. Butterworth-Heinemann.
- Davies, R.M., Taylor, G.I., 1950. The mechanics of large bubbles rising through liquids in tubes. *Proc. Roy. Soc. Lond. Ser.-A, Math. Phys. Sci.* 200 (1062), 375–390.
- Deshpande, S.S., Anumolu, L., Trujillo, M.F., 2012. Evaluating the performance of the two-phase flow solver interFoam. *Comput. Sci. Discov.* 5, 014016.
- Dumitrescu, D.T., 1943. Strömung an einer Luftblase im senkrechten Rohr. *Z. Angew. J. Appl. Math. Mech.* 23, 139–149.
- El-Sayed, E.E.F., 1984. Pulsating Flow of Non-Newtonian Fluids in Pipes, Ph.D. Thesis. McMaster University, Hamilton, Canada.
- Focke, C., Bothe, D., 2011. Computational analysis of binary collisions of shear-thinning droplets. *J. NonNewton. Fluid Mech.* 166, 799–810.
- Funfschilling, D., Li, H.Z., 2001. Flow of non-Newtonian fluids around bubbles: PIV measurements and birefringence visualisation. *Chem. Eng. Sci.* 56, 1137–1141.
- Haddad, K., Ertunc, O., Mishra, M., Delgado, A., 2010. Pulsating laminar fully developed channel and pipe flows. *Phys. Rev. E* 81, 016303.
- Hassager, O., 1979. Negligible wake behind bubbles in non-Newtonian liquids. *Nature* 279, 402–403.
- Herrera-Velarde, J.R., Zenit, R., Chehata, D., Mena, B., 2003. The flow of non-Newtonian fluids around bubbles and its connection to the jump discontinuity. *J. NonNewton. Fluid Mech.* 111 (2–3), 199–209.
- Hewson, R.W., Kapur, N., Gaskell, P.H., 2009. A model for film-forming with Newtonian and shear-thinning fluids. *J. NonNewton. Fluid Mech.* 162, 21–28.
- Johnson, A.B., White, D.B., 1993. Experimental determination of gas migration velocities with non-Newtonian fluids. *Int. J. Multiph. Flow* 19 (6), 921–941.
- Kajero, O.T., Azzopardi, B.J., Abdulkareem, L., 2012. Experimental investigation of the effect of liquid viscosity on slug flow in small diameter bubble column. In: EPJ Web of Conferences, vol. 25, article number: 01037.
- Kamislı, F., Ryan, M.E., 1999. Perturbation method in gas-assisted power-law fluid displacement in a circular tube and a rectangular channel. *Chem. Eng. J.* 75 (3), 167–176.
- Kang, C.W., Quan, S., Lou, J., 2010. Numerical study of a Taylor bubble rising in stagnant liquids. *Phys. Rev. E*, 81, 066308.
- Karamanov, D.G., 2001. The study of free rise of buoyant spheres in gas reveals the universal behaviour of free rising rigid spheres in fluid in general. *Int. J. Multiph. Flow* 27 (8), 1479–1486.
- Kubie, J., 2000. Velocity of long bubbles in horizontally oscillating vertical pipes. *Int. J. Multiph. Flow* 26 (2), 339–349.
- Lee, B.B., Chan, E.S., Ravindra, P., Khan, T.A., 2012. Surface tension of viscous biopolymer solutions measured using du Nouy Rind method and drop weight methods. *Polym. Bull.* 69 (4), 471–489.
- Li, S., Ma, Y., Fu, T., Zhu, C., Li, H., 2012. The viscosity distribution around a rising bubble in shear-thinning non-Newtonian fluids. *Braz. J. Chem. Eng.* 29 (2), 265–274.
- Liberzon, D., Shemer, L., Barnea, D., 2006. Upward-propagating capillary waves on the surface of short Taylor bubbles. *Phys. Fluids* 18, 048103.
- Madani, S., Caballina, O., Souhar, M., 2009. Unsteady dynamics of Taylor bubble rising in vertical oscillating tubes. *Int. J. Multiph. Flow* 35, 363–375.
- Maeda, N., 1975. Behavior of a single bubble in a quiescent and following liquid inside a cylindrical tube. *J. Nucl. Sci. Technol.* 12 (10), 606–617.
- Margaritis, A., Bokkel, D.W.T., Karamanov, D.G., 1999. Bubble rise velocities and drag coefficients in non-Newtonian polysaccharide solutions. *Biotechnol. Bioeng.* 64 (3), 257–266.
- Marschall, H., Boden, S., Lehrenfeld, C., Falconi, D.C.J., Hampel, U., Reusken, A., Worner, M., Bothe, D., 2014. Validation of interface capturing and tracking techniques with different surface tension treatments against a taylor bubble benchmark problem. *Comp. Fluids* 102, 336–352.
- Nicklin, D.J., Wilkes, J.O., Davidson, J.F., 1962. Two-phase flow in vertical tubes. *Trans. Inst. Chem. Eng.* 40, 61–68.
- Nogueira, S., Riethmüller, M.L., Campos, J.B.L.M., Pinto, A.M.F.R., 2005. Flow in the nose region and annular film around a Taylor bubble rising through vertical columns of stagnant and flowing Newtonian liquids. *Chem. Eng. Sci.* 61 (2), 845–857.
- Quan, S., 2011. Co-current flow effects on a rising Taylor bubble. *Int. J. Multiph. Flow* 37, 888–897.
- Sousa, R.G., Riethmüller, M.L., Pinto, A.M.F.R., Campos, J.B.L.M., 2005. Flow around individual Taylor bubbles rising in stagnant CMC solutions: PIV measurements. *Chem. Eng. Sci.* 60, 1859–1873.
- Sousa, R.G., Pinto, A.M.F.R., Campos, J.B.L.M., 2007. Interaction between Taylor bubbles rising in stagnant non-Newtonian fluids. *Int. J. Multiph. Flow* 33, 970–986.
- Thermophysical Properties of Fluid Systems. NIST Standard Reference Database <[webbook.nist.gov/chemistry/fluid](http://webbook.nist.gov/chemistry/fluid)> (retrieved 02.14).
- Tomiyama, A., Celata, G.P., Hosokawa, S., Yoshida, S., 2002. Terminal velocity of single bubbles in surface tension force dominant regime. *Int. J. Multiph. Flow* 28 (9), 1497–1519.
- Tong, B.Y., Wong, T.N., Ooi, K.T., 2001. Closed-loop pulsating heat pipe. *Appl. Therm. Eng.* 21 (18), 1845–1862.
- Ubbink, O., 1997. Numerical Prediction of Two Fluid Systems with Sharp Interfaces, Ph.D. Thesis. Imperial College of Science, Technology & Medicine, London, United Kingdom.
- Ubbink, O., Issa, R.I., 1999. A method for capturing sharp fluid interfaces on arbitrary meshes. *J. Comput. Phys.* 153 (1), 26–50.
- Uno, S., Kintner, R.C., 1956. Effect of wall proximity on the rate of rise of single air bubbles in a quiescent liquid. *Am. Inst. Chem. Eng. J.* 2 (3), 420–425.
- Zalesak, S.T., 1979. Fully multidimensional flux-corrected transport algorithms for fluids. *J. Comput. Phys.* 31, 335–362.